To the Graduate Council:

I am submitting herewith a thesis written by William Campbell Moonan entitled "Evaluation of the Aerodynamics of an Aircraft Fuselage Pod Using Analytical, CFD, and Flight Testing Techniques". I have examined the final electronic copy of this thesis for form and content and recommend that it be accepted in partial fulfillment of the requirements for the degree of Master of Science, with a major in Engineering Science.

John F. Muratore
Major Professor

We have read this thesis
and recommend its acceptance:

Borja Martos

U. Peter Solies

Acceptance for the Council:

Carolyn R. Hodges
Vice Provost and Dean
of the Graduate School

(Original signatures are on file with official student records.)

EVALUATION OF THE AERODYNAMICS OF AN AIRCRAFT FUSELAGE POD USING ANALYTICAL, CFD, AND FLIGHT TESTING TECHNIQUES

A Thesis
Presented for the
Master of Science
Degree
The University of Tennessee, Knoxville

William Campbell Moonan
December 2010

ACKNOWLEDGMENTS

I wish to thank everyone who helped me throughout my pursuit of my Master of Science in Engineering Science. I would like to thank Professor Muratore for his patient guidance and steady encouragement through the process. I would like to thank Professor Martos and Dr. Corda for helping me create testing procedures, gather data, and interpret results. I would also like to thank Dr. Solies for serving on my thesis committee.

I would especially like to thank Joe Young for his patience and friendship over the past two years, for constantly letting me run ideas by him, and for finding the mistakes that I could not.

ABSTRACT

The purpose of this study is to investigate the execution and validity of various predictive methods used in the design of the aerodynamic pod housing NASA's Marshall Airborne Polarimetric Imaging Radiometer (MAPIR) on the University of Tennessee Space Institute's Piper Navajo research aircraft. Potential flow theory and wing theory are both used to analytically predict the lift the MAPIR Pod would generate during flight; skin friction theory, empirical data, and induced drag theory are utilized to analytically predict the pod's drag. Furthermore, a simplified computational fluid dynamics (CFD) model was also created to approximate the aerodynamic forces acting on the pod. A limited flight test regime was executed to collect data on the actual aerodynamic effects of the MAPIR Pod. Comparison of the various aerodynamic predictions with the experimental results shows that the assumptions made for the analytic and CFD analyses are too simplistic; as a result, the predictions are not valid. These methods are not proven to be inherently flawed, however, and suggestions for future uses and improvements are thus offered.

TABLE OF CONTENTS

I. BACKGROUND……. 1
II. POTENTIAL FLOW ANALYSIS LIFT PREDICTIONS……..4
III. WING THEORY LIFT PREDICTIONS…….7
IV. DRAG THEORY PREDICTIONS…… 13
V. CFD ANALYSIS PREDICTIONS…… 16
VI. FLIGHT TESTING……22
VII. RESULTS AND DISCUSSION…… 31
VIII. RECOMMENDATIONS FOR FUTURE ANALYSIS…….....35
IX. CONCLUSION……..36
LIST OF REFERENCES……...37
APPENDICES……39
A1. DERIVATION OF POD LIFT COEFFICIENT USING IDEAL FLOW THEORY…….....40
A2. CFD ANALYSIS SPECIFICATIONS…….. 43
A3. FLIGHT TESTING……45
Angle of Sideslip Calibration…….....45
Engine Performance Graphs…….. 48
Sample Flight Test Calculations…… 50
VITA…….. 53

LIST OF TABLES

3.1. Summary of MAPIR Pod C_{L_α} and Lift Curve Equations Using Various Wing Theory Techniques and Potential Flow Results…….....11

4.1. Summary of MAPIR Pod Parasite and Induced Drag Values for Various Predictive Techniques……...15

A2.1. CFD PC Specifications for MAPIR Pod Analysis……...43

A2.2. Summary of MAPIR Pod CFD Cases……..44

LIST OF FIGURES

1.1. Piper Navajo and MAPIR Instrument Dimensions……2
1.2. Piper Navajo N11UT with MAPIR Pod Installed……..3
2.1. Side Profile of MAPIR Pod for Potential Flow Analysis…….. 4
3.1. Theoretical Lift Curve Slope vs. Wing Thickness Ratio……..... 8
3.2. Geometry Factor K vs. Trailing Edge Geometry for Various Reynolds Numbers……..... 9
3.3. Determination of Three-Dimensional Wing Lift Curve Slope…….. 9
3.4. Coefficient of Lift C_L vs. Angle of Attack α for MAPIR Pod Wing Theory Approximations……..12
4.1. Interference Drag Coefficient for Rounded Tapered Bodies……...15
5.1. CFD Analysis Geometry……..18
5.2. Total Force vs. Iteration for MAPIR Pod CFD Analysis…….....19
5.3. Coefficient of Lift C_L and Coefficient of Drag C_D vs. Angle of Attack α for MAPIR Pod CFD Analysis…….....20
5.4. Coefficient of Lift C_L vs. Coefficient of Drag C_D for MAPIR Pod CFD Analysis……21
6.1. Force Balance of Aircraft in Steady Flight…….. 23
6.2. Altitude Position Error Correction ΔH_{pc} vs. Indicated Airspeed V_{iw} for MAPIR Pod Flight Testing……... 25
6.3. Velocity Position Error Correction ΔV_{pc} vs. Indicated Airspeed V_{iw} for MAPIR Pod Flight Testing……... 25
6.4. Pitch Attitude θ vs. Indicated Angle of Attack α for MAPIR Pod Flight Testing……26
6.5. True Sideslip Angle β_{true} vs. Measured Sideslip Angle $\beta_{measured}$ for MAPIR Pod Flight Testing Using AGARD AOSS Calibration Technique…….. 26
6.6. Coefficient of Lift C_L and Coefficient of Drag C_D vs. Angle of Attack α for MAPIR Pod Flight Testing……..... 30
6.7. Coefficient of Drag C_D vs. Coefficient of Lift C_L for MAPIR Pod Flight Testing……30
7.1. Coefficient of Lift C_L vs. Angle of Attack α for MAPIR Pod Analytic Predictions, CFD Predictions, and Flight Testing…….....31
7.2. Coefficient of Drag C_D vs. Angle of Attack α for MAPIR Pod Analytic Predictions, CFD Predictions, and Flight Testing……..... 32
7.3. Coefficient of Drag C_D vs. Angle of Attack α for MAPIR Pod CFD Predictions and Flight Testing……..... 33
7.4. Coefficient of Drag C_D vs. Coefficient of Lift C_L for MAPIR Pod Analytic Predictions, CFD Predictions, and Flight Testing……. 33
A1.1. Side Profile of MAPIR Pod for Potential Flow Analysis……..... 40
A2.1. CFD Analysis Geometry……..43
A3.1. Regression to Find Proportionality Constant K in AGARD AOSS Calibration Equation $\beta_{meas} = \beta_0 + K\beta_{true} - Error\ Terms$

(Pod-on Data)……...47
A3.2. Lycoming Aircraft Engine Performance Data – 2575 RPM……48
A3.3. Lycoming Aircraft Engine Performance Data – 2400 RPM……49
A3.4. Lycoming Aircraft Engine Performance Data – 2200 RPM……49

ABBREVIATIONS AND SYMBOLS

α	Angle of Attack
β	Angle of Side Slip
θ	Pitch Angle
ρ	Density
A	Wing Aspect Ratio
b	Wingspan
c	Wing Chord
C_D	Drag Coefficient
C_f	Force Coefficient
C_L	Lift Coefficient
C_{L_α}	Lift Curve Slope
C_p	Pressure Coefficient
CFD	Computational Fluid Dynamics
D	Drag
DAS	Data Acquisition System
e	Oswald Span Efficiency
FTE	Flight Test Engineer
L	Lift
M	Mach Number
MAPIR	Marshall Airborne Polarimetric Imaging Radiometer
MSFC	Marshall Space Flight Center
OML	Outer Mold Line
p	Pressure
q	Dynamic Pressure
Re	Reynolds Number
S	Reference Area
S_{wet}	Wetted Surface Area
T	Thrust
UTSI	University of Tennessee Space Institute
V	Airspeed
W	Weight
Y	Lateral Force

CHAPTER I
BACKGROUND

In an ideal world, aircraft would be designed from the outset with all possible missions in mind; as such, modifications would never need to be made to the vehicle to accommodate changing requirements. This, of course, is not the case; aircraft designed for a particular requirement are often modified to handle drastically different missions as their operators' needs evolve.

Given the highly complex nature of aircraft, any proposed modification must be thoroughly designed and rigorously tested prior to any flight operation. Changes to an aircraft's outer mold lines (OML) will inherently disrupt the way air flows over the vehicle. Such disruptions in airflow can range from negligible to drastic; however, it is not their magnitude that is of concern, but rather their effect on the performance and handling characteristics of the modified aircraft. In extreme cases, modifications to the OML can degrade the flight characteristics enough to yield a vehicle that is no longer safe to operate.

Many methods exist for predicting the influence OML modification will have on an aircraft's flight characteristics. Hand calculations using simplified assumptions of aircraft geometries and flow properties and using empirical data can yield approximate, first-order results. Wind tunnel testing can yield very accurate predictions, but such tests are usually very expensive and require specialized facilities. Computational fluid dynamics (CFD) analysis is becoming much more common given the ever-increasing speed and improving capabilities of computers; however, CFD predictions must balance speed of computation with accuracy of results. Simplified models will inherently run faster, but the results will be less accurate than a more detailed simulation that takes more time to solve.

Ideally these methods are applied to the design process iteratively; what starts out as a rough design will converge on an aerodynamically refined OML that both meets the mission requirements as well as limits the effects on the aircraft's flight characteristics. Such an iterative engineering approach necessarily can take significant time, resources, and specialized facilities; when schedules and funding are tight, the extra time needed to yield aerodynamically clean designs may be reduced or eliminated in favor of meeting more important mission goals. What results is a product that fulfills its mission requirements and yields safe flight operations, but may influence an aircraft's performance more than desired. The University of Tennessee Space Institute's (UTSI) Aviation Systems and Flight Research Department undertook such a mission, applying the highest technology possible with the limited resources available to meet all the mission goals.

NASA's Marshall Space Flight Center (MSFC) developed a large, phased-array sensor able to very accurately measure surface temperatures from altitude. MSFC wished to evaluate this Marshall Airborne Polarimetric Imaging Radiometer (MAPIR) on one of the Aviation Systems Department's aircraft. The department chose the largest aircraft in its fleet for this task: a Piper PA-31 Navajo already heavily instrumented for flight test

instruction. Figure 1.1 shows the dimensions of both a Piper Navajo and the MAPIR instrument.

The MAPIR mission called for numerous aircraft system additions and upgrades, as well as a significant modification of the Navajo's OML through the addition of fairings to house the MAPIR on the aircraft's fuselage.

The design of these fairings was driven by a number of factors, some of which were competing. The sensor's size dictated that any fairing developed had to be at least as large as the MAPIR plus any mounting system created to hang the sensor from the aircraft. For stability and control considerations, the MAPIR needed to be mounted low and forward of the center of gravity of the aircraft, but the Navajo had no existing external system, such as hard-points, for affixing the MAPIR anywhere on the fuselage.

These structural and location limitations therefore applied a number of constraints on the possible shapes for the fairing OML. Further restricting the fairing shape was the need for the structures to be relatively easily manufactured. Finally, limited funding and an accelerated schedule additionally complicated matters.

All these constraints entailed that the iterative approach to refining the aerodynamic design of the fairings had to be severely limited; no wind tunnel facilities could be used in their development, and any CFD analysis had to be heavily simplified for time constraints and because no accurate computer model of the Navajo existed. Structural, manufacturing, and integration concerns thus took precedence over the effects aerodynamic inefficiencies might have on the aircraft performance, as long as any degradations did not lead to unsafe flight operations.

The fairing OML was thus finalized, allowing limited CFD analysis to be run to try and predict loading on the assembly. These results translated into the structural design

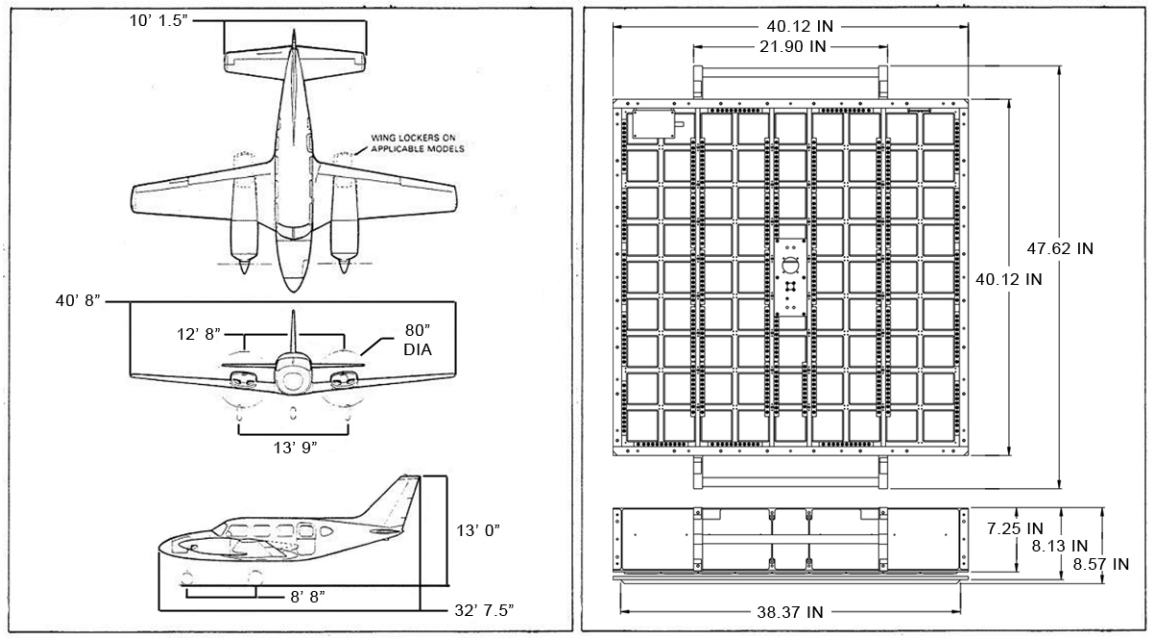

Figure 1.1 – Piper Navajo (left) and MAPIR Instrument (right) Dimensions

and manufacturing of the fairings, followed by a rigorous ground structural-test regime and flight-test regime that cleared the fairing-MAPIR assembly, or MAPIR Pod, for flight operations. Figure 1.2 shows the MAPIR Pod installed on UTSI's Navajo N11UT.

The success of the MAPIR mission proves that a non-iterative, accelerated design approach to modifying an aircraft's OML is possible; however, this success does nothing to illustrate the accuracy of the predictions one could employ in such an accelerated design. Thus, what follows is an investigation of analytic and CFD methods, and how to determine their validity, using the limited-resource, non-iterative approach employed in the MAPIR mission as an example.



Figure 1.2 - Piper Navajo N11UT with MAPIR Pod Installed

CHAPTER II
POTENTIAL FLOW ANALYSIS LIFT PREDICTIONS

All fluid flows are governed by the Navier-Stokes equations; however, finding closed-form solutions to these highly non-linear equations can be nearly impossible except for the most basic of flow fields. Simplifying assumptions can be made to further expand the applicability of the Navier-Stokes equations, but such simplifications limit the accuracy of the results. One such simplification is for incompressible, isothermal, two-dimensional high Reynolds number flows.

Ideal, or potential, flows occur when viscous effects within the fluid are negligible; this can only occur at high Reynolds numbers. Furthermore, ideal flows require that flow is irrotational, or that the vorticity is zero. Therefore, ideal flows cannot predict the drag on a body, because drag results from viscous effects such as skin friction and flow separation. However, they can predict pressure force changes in fluid velocities within the field, and therefore are useful for estimating the lift or suction around a body.

Such flows do not actually exist in nature, but close approximations do occur, such as for certain aircraft bodies in flight. In this situation, the oncoming flow field is at a high Reynolds number and is irrotational. When the flow encounters the aircraft bodies, the vorticity generated is confined to a thin viscous boundary layer near the surface.

Despite these simplifying assumptions, potential flow analysis is still heavily limited by geometry. To achieve analytical results, only simple geometries can be considered. For the case of the MAPIR Pod, this is not a concern; because of manufacturing considerations, the pod OML was chosen to be quite simple, composed of only flat and circular sections, with no complex geometries. The actual MAPIR Pod has tapered forward and aft fairings, but for this potential flow analysis only two-dimensional geometries will be considered, then expanded to a three-dimensional result. Figure 2.1 illustrates the dimensions of the two-dimensional cross-section of the MAPIR Pod used in this analysis.

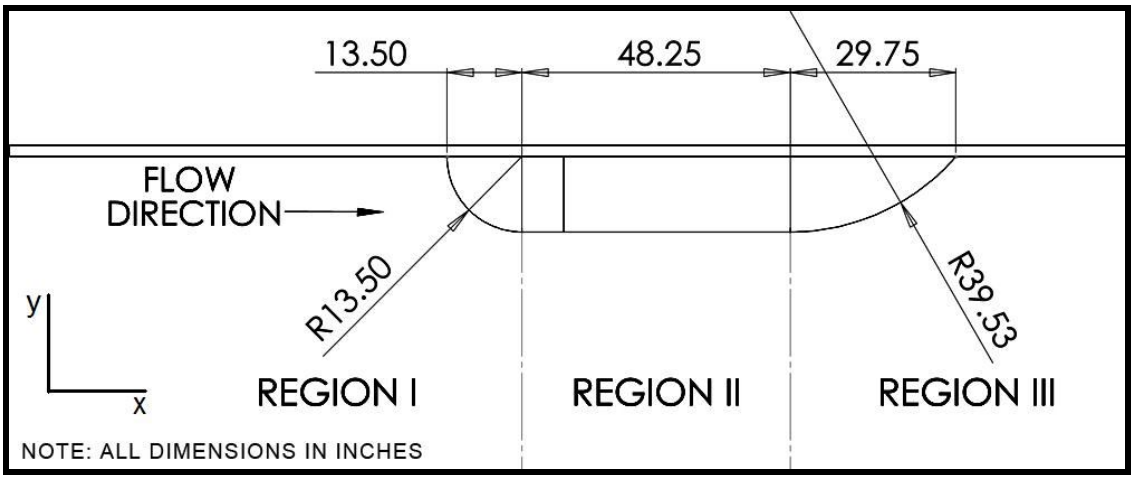

FIGURE 2.1 - Side Profile of MAPIR Pod for Potential Flow Analysis

To find the pressure distribution, and thus the lift, along this profile, the analysis will be broken up into three sections: flow up the front quarter of a cylinder (Region I), flow over a flat plate (Region II), and flow over a portion of the back of a cylinder (Region III).

Potential flow theory for flow over a cylinder (Panton, 423) gives radial and tangential components of the velocity field of

$$v_r = V\left(1-\frac{r_0^{\,2}}{r^2}\right)\cos\theta \qquad v_\theta = -V\left(1+\frac{r_0^{\,2}}{r^2}\right)\sin\theta \tag{2.1}$$

It is important to note that the fluid flow has only a radial component at $\theta = 0$ and $\theta = \pi$; this yields streamlines in the flow field and stagnation points on the cylinder surface at these angles. By definition the fluid velocity is tangential to a streamline, and thus fluid cannot pass through a streamline (Panton, 251). The presence of the flat plate, representing the aircraft fuselage, upstream of the forward cylinder is therefore irrelevant for potential flow analysis because it lies on the $\theta = \pi$ streamline; the analysis for this situation is identical to potential flow theory for a cylinder with no such plate.

The flat plate behind the aft cylinder, however, does not lie on a stagnation streamline; therefore, that surface's presence would have an effect on the upstream potential flow field. This discrepancy, however, will be neglected so that analytic solutions to the ideal flow analysis may be determined.

At the cylinder surface, the radial velocity component is zero and the tangential velocity component simplifies to

$$v_\theta = -2V\sin\theta \tag{2.2}$$

Thus, the two-dimensional coefficient of pressure along a cylinder's surface is

$$C_{p_{circ}} = \frac{p-p_\infty}{\frac{1}{2}\rho V^2} = 1-4\sin^2\theta \tag{2.3}$$

By definition pressure acts normal to a surface; positive pressures therefore act to "push in" a surface and negative pressures act to "pull out" a surface.

To find the two-dimensional lift coefficient for a cylindrical section from this pressure coefficient, the component of $C_{p_{circ}}$ in the lift direction (positive y-direction) must be determined, and then integrated along the given profile's length. Therefore,

$$C_{p_y} = C_p\left(-\sin\theta\right) = -\sin\theta + 4\sin^3\theta \tag{2.4}$$

$$C_{L_{2D}} = \int\left(-\sin\theta + 4\sin^3\theta\right)r\,d\theta \tag{2.5}$$

For Region I, equation 2.5 is integrated from π to $3\pi/2$ with $r = r_{fwd}$ = 13.5 in; for Region III, it is solved from $3\pi/2$ to 0.2288π with $r = r_{aft}$ = 39.53 in. This yields forward and aft two-dimensional lift coefficients of $C_{L_{2D_{fwd}}}$ = -1.875 and $C_{L_{2D_{aft}}}$ = -4.3516, respectively.

The flow over Region II is determined by the flow at the boundary between Region I and Region II. Thus, $C_{p_{circ}}\left(\theta = 3\pi/2\right) = -3$. This is then integrated along the length of Region II to yield a two-dimensional lift coefficient of $C_{L_{2D_{flat}}} = -12.0625$.

The two-dimensional lift for the whole profile is then the sum of the lift coefficients for each region multiplied by the dynamic pressure q.

$$\begin{aligned} L_{2D_{pod}} &= q\left(C_{L_{2D_{fwd}}} + C_{L_{2D_{flat}}} + C_{L_{2D_{aft}}}\right) \\ &= q\left(-1.875 - 12.0625 - 4.3516\right) = -18.2891q \end{aligned} \tag{2.6}$$

This is multiplied by the pod's span to yield a three-dimensional pod lift value.

$$L_{pod} = qbL_{2D_{pod}} = q\left(3.4267\right)\left(-18.2891\right) = -62.6713q \tag{2.7}$$

This can then be converted to a total potential flow lift coefficient for the pod:

$$S_{pod_{theory}} = b_{pod}c_{pod} = \left(3.4267 \text{ ft}\right)\left(7.625 \text{ ft}\right) = 26.1284 \text{ ft}^2 \tag{2.8}$$

$$C_{L_{pod}} = \frac{L_{pod}}{qS_{pod_{theory}}} = \frac{-62.6713q}{\left(26.1284\right)q} = -2.3986 \tag{2.9}$$

A complete derivation of $C_{L_{pod}}$ can be found in Appendix A1.

The assumptions made to find the pod lift coefficient using potential flow theory are significant, and therefore worth explicitly restating. It was assumed that the incoming flow was non-vorticle and at a high Reynolds number, allowing the viscous effects to be neglected everywhere but a thin boundary layer near the pod surface. The analysis was done for an axis-symmetric, two-dimensional profile that was then expanded into a finite three-dimensional shape; this shape differed from the actual MAPIR Pod geometry. The fuselage of the aircraft was approximated by flat plates both upstream and downstream of the pod profile. The effects of the downstream flat plate were ignored; as discussed, the presence of this plate would change the flow properties and thus the pressure distribution upstream.

Furthermore, the flow was assumed to stay attached for the entire length of the pod; in truth, this is unrealistic. Flows over cylinders are prone to separation past 90°, resulting in low pressure regions downstream of the cylinder. (Panton, 423) This type of separated flow results in much larger wake drag. While this is a viscous effect, and therefore cannot be predicted by potential flow theory, such a wake would invariably change the overall pressure distribution on the aft fairing, in turn altering the lift coefficient for this body.

Also, casual inspection of equation 2.1 and equation 2.2 highlights the limitations of this analysis for the MAPIR Pod geometry. At $\theta = 3\pi/2$, equation 2.2 gives identical flow values for both Region I and Region III. However, at the same angle but at distances beyond the cylinders' surfaces, equation 2.1 gives differing flow values; this results from the discrepancy between $r_o = r_{fwd}$ in Region I and $r_o = r_{aft}$ in Region II. This illustrates that this analysis is not truly realistic for the MAPIR Pod geometry. However, because the pressure distribution of interest acts at the cylinders' surfaces, this discontinuity will be neglected to yield the rough approximations desired.

CHAPTER III
WING THEORY LIFT PREDICTIONS

The geometry of the MAPIR Pod cross-section is similar to a negatively-cambered airfoil resting on a flat plate; wing theory therefore will be utilized to try and predict the lift produced by the simplified MAPIR Pod geometry used in the potential flow analysis.

Wings have lift curves that change linearly with angle of attack up until the region of stall; uncambered wings produce no lift at zero angle of attack, while cambered wings create some non-zero lift at zero angle of attack. Thus, the total lift generated by a wing can be characterized by:

$$C_L = C_{L_0} + C_{L_\alpha}\alpha \tag{3.1}$$

For airfoils, or wings with theoretically infinite aspect ratios (infinite spans), the slope of this curve C_{L_α} is equal to 2π rad^{-1}. Trailing vortices and other three-dimensional effects reduce this lift curve slope for finite wings; the smaller the aspect ratio of a wing, the more significant the decrease. (Raymer, 310)

There exist a number of methods to predict C_{L_α} for a given wing. The simplest augmentation to the airfoil prediction of 2π is:

$$C_{L_\alpha} = 2\pi \frac{A}{2 + A} \tag{3.2}$$

where *A* is the wing aspect ratio. If the MAPIR Pod is treated as a very short, negatively-cambered wing, equation 3.2 yields:

$$A = \frac{{b_{pod}}^2}{S_{pod_{theory}}} = \frac{\left(3.4267 \text{ ft}\right)^2}{\left(26.1284 \text{ ft}^2\right)} = 0.4494$$

$$C_{L_\alpha} = 2\pi \frac{A}{2 + A} = 2\pi \frac{\left(0.4494\right)}{\left(2.4494\right)} = 1.1528 \text{ rad}^{-1} = 0.02012 \text{ deg}^{-1}$$

Etkin expands this modification to include flow property effects, airfoil geometry effects, and compressibility effects. (Etkin, 320) His process first requires determination of a theoretical two-dimensional lift curve slope $C_{l_{\alpha_{theory}}}$ based on the airfoil thickness ratio *t/c* and the Reynolds number of the flow being considered. Figure 3.1 is a reproduction of Etkin's method (Etkin, 321) for finding the theoretical two-dimensional lift curve slope.

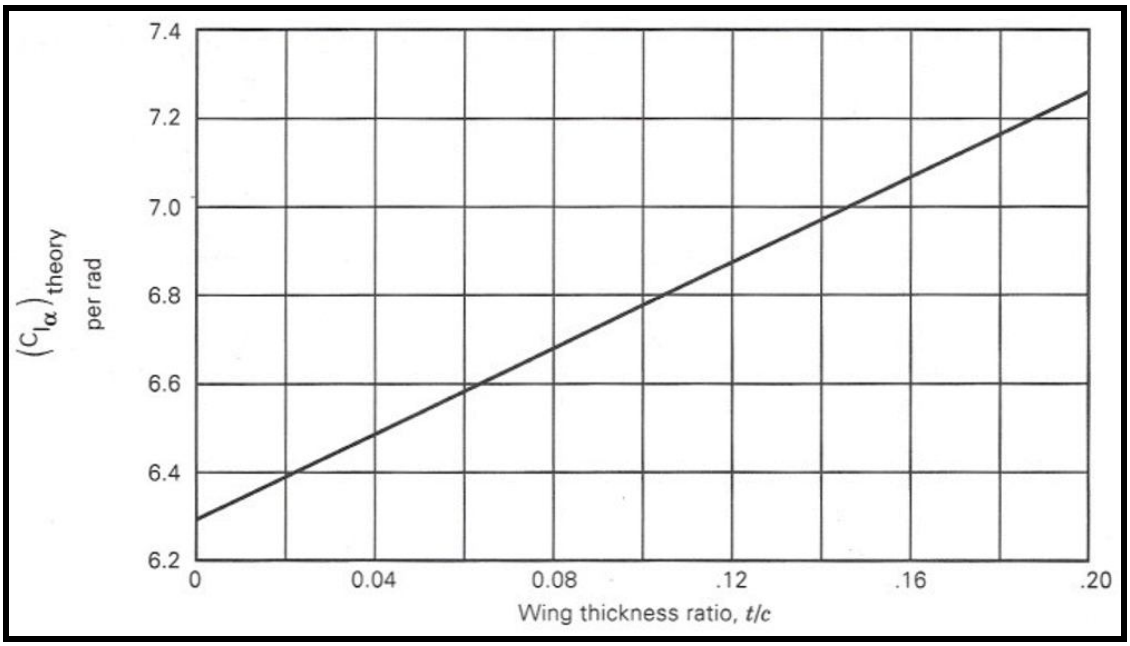

Figure 3.1 – Theoretical Lift Curve Slope vs. Wing Thickness Ratio

$C_{l_{\alpha_{theory}}}$ is then modified by a compressibility factor β and a geometry factor K:

$$C_{l_\alpha} = \frac{1.05}{\beta} K C_{l_{\alpha_{theory}}} \tag{3.3}$$

where $\beta = \sqrt{1-M^2}$ and K is graphically determined from Figure 3.2 (Etkin, 321) using the trailing-edge geometry of the airfoil, where

$$\tan\frac{1}{2}\phi_{TE}' = \frac{\frac{1}{2}\left(Y_{90} - Y_{99}\right)}{9} \tag{3.4}$$

In this equation, ϕ_{TE} is the trailing-edge angle of the airfoil, and Y_{90} and Y_{99} are the airfoil thicknesses at 90% and 99% of the chord length, respectively.

The three-dimensional wing lift curve slope C_{L_α}, which includes the effects of finite aspect ratios, is then found graphically from Figure 3.3 (Etkin, 322), where

$$\kappa = \frac{\beta C_{l_\alpha}}{2\pi} \tag{3.5}$$

and $\Lambda_{c/2}$ is defined as the sweep-angle of the wing half-chord line.

Once again the MAPIR Pod will be treated as a low-aspect ratio wing and the Etkin equations will be applied to determine the lift-curve slope. Because the initial two-dimensional theoretical slope $C_{l_{\alpha_{theory}}}$ relies on Reynolds number, an average Reynolds number must be determined that embodies the typical flow conditions encountered by the pod; therefore, an airspeed of 130 mph is chosen (this is the average airspeed used in the flight testing of the pod). Furthermore, a length scale other than the pod chord length

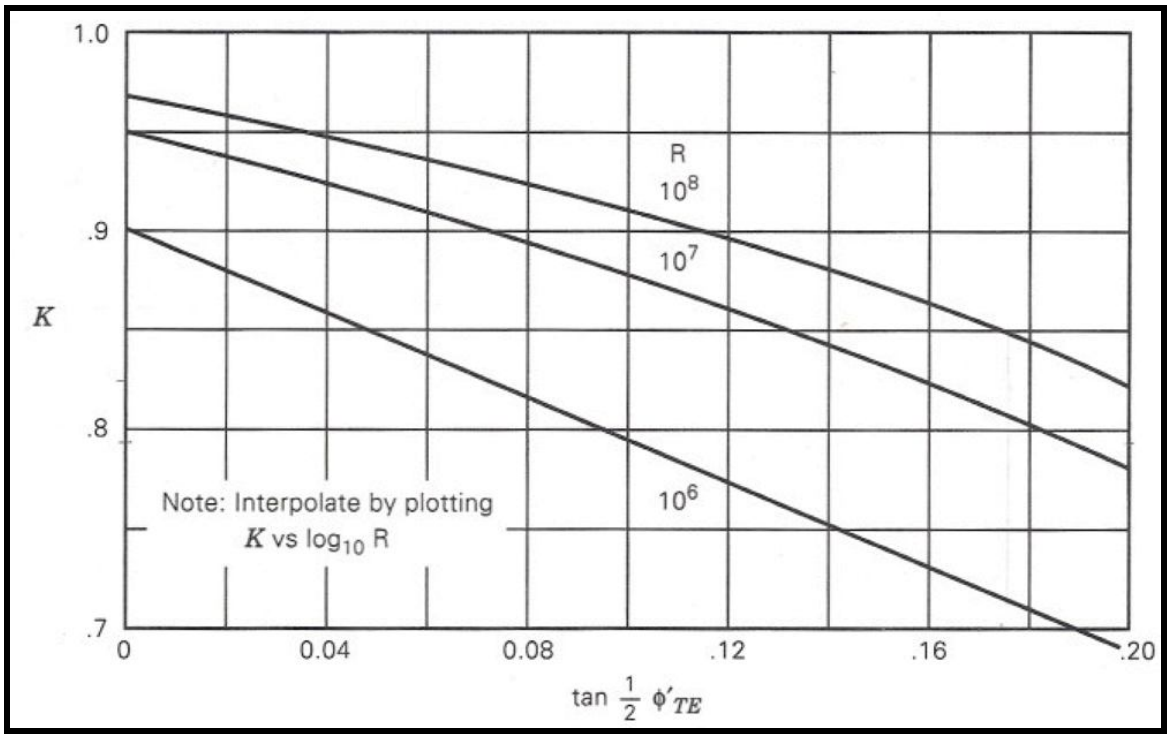

Figure 3.2 – Geometry Factor *K* vs. Trailing Edge Geometry for Various Reynolds Numbers

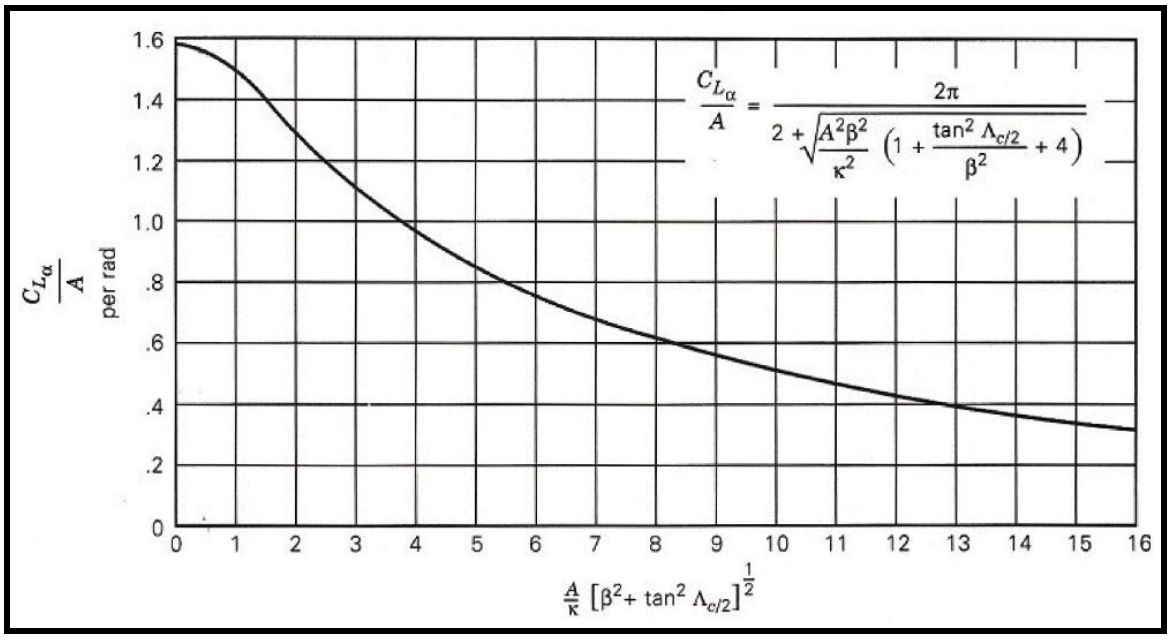

Figure 3.3 – Determination of Three-Dimensional Wing Lift Curve Slope

must be used. While a wing encounters free-stream flow at its leading edge, the MAPIR Pod is attached to the fuselage of the aircraft. Thus, the incoming flow is already energized by the length of fuselage forward of the pod's leading edge. This length will therefore be added to the pod chord length to determine the pod Reynolds number for use in Figure 3.1.

$$\begin{aligned}\mathrm{Re}_{avg} &= \frac{\left(L_{fuselage} + C_{pod}\right)V}{\nu} \\ &= \frac{\left(10.1667\text{ ft} + 7.625\text{ ft}\right)\left(130\text{ mph}\right)\left(1.4667\text{ fps/mph}\right)}{\left(157.2\times10^{-6}\text{ ft}^2/\text{s}\right)} \\ &= 2.158\times10^{7}\end{aligned}$$

The pod thickness ratio is

$$\frac{t}{c} = \frac{13.5\text{ in}}{91.5\text{ in}} = 0.1475$$

Figure 3.1 therefore yields $C_{l_{\alpha_{theory}}} = 7.01\text{ rad}^{-1}$.

Using the geometry of the MAPIR Pod, equation 3.4 yields:

$$\tan\frac{1}{2}\phi_{TE}' = \frac{\frac{1}{2}\left(Y_{90} - Y_{99}\right)}{9} = \frac{\frac{1}{2}\left(8.424 - 1.103\right)}{9} = 0.4067$$

This value, however, is off the scale of Figure 3.2. Furthermore, as discussed with regards to the potential flow analysis, flow over the aft portion of a cylinder tends to separate from the cylinder surface quickly past 90°. Equation 3.3 gives $\phi_{TE} = 44.26^{\circ}$; therefore, using the geometry of the pod at 90% and 99% of the chord is invalid because the flow would not be attached in this region. Instead, a trailing edge angle of $\phi_{TE} = 22.61^{\circ}$ is chosen, resulting in

$$\tan\frac{1}{2}\phi_{TE}' = 0.2$$

Figure 3.2 therefore gives $K = 0.795$. β is easily calculated:

$$\beta = \sqrt{1 - M^2} = \sqrt{1 - \frac{\left(130\text{ mph}\right)\left(1.4667\text{ fps/mph}\right)}{\left(1116\text{ fps}\right)}} = 0.9853$$

Equation 3.3 thus gives the modified two-dimensional lift curve slope as:

$$C_{l_\alpha} = \frac{1.05}{0.9853}\left(0.795\right)\left(7.01\right) = 5.939\text{ rad}^{-1} = 0.1037\text{ deg}^{-1}$$

To determine the three-dimensional lift curve slope, κ is first calculated to be:

$$\kappa = \frac{\beta C_{l_\alpha}}{2\pi} = \frac{\left(0.9853\right)\left(5.939\text{ rad}^{-1}\right)}{2\pi} = 0.9319\text{ rad}^{-1}$$

The pod is assumed to have zero wing-sweep; thus:

$$\frac{A}{\kappa}\left[\beta^2 + \tan^2\Lambda_{c/2}\right]^{1/2} = \frac{\left(0.4494\right)}{\left(0.9319\text{ rad}^{-1}\right)}\left[\left(0.9853\right)^2 + \tan^2\left(0\right)\right]^{1/2} = 0.4755\text{ rad}$$

Figure 3.3 then gives:

$$\frac{C_{L_\alpha}}{A} = 1.5538 \text{ rad}^{-1}$$

$$\therefore C_{L_\alpha} = 0.6983 \text{ rad}^{-1} = 0.01219 \text{ deg}^{-1}$$

Etkin also gives a semi-empirical formula for determining the three-dimensional lift curve slope of a wing. (Etkin, 322) As with the above analysis, this equation uses the wing aspect ratio, compressibility effects, and sweep angle to modify the two-dimensional lift curve slope.

$$\frac{C_{L_{\alpha_{Raymer}}}}{A} = \frac{2\pi}{2 + \sqrt{\frac{A^2\beta^2}{\kappa^2}\left(1 + \tan^2 \Lambda_{c/2} + 4\right)}} \tag{3.6}$$

For the MAPIR Pod, κ and β are identical to that calculated above. Thus, equation 3.6 gives:

$$\frac{C_{L_\alpha}}{A} = 2.0512 \text{ rad}^{-1}$$

$$\therefore C_{L_\alpha} = 0.9218 \text{ rad}^{-1} = 0.01609 \text{ deg}^{-1}$$

Table 3.1 summarizes the values of C_{L_α} and resulting lift curve equations using the three techniques discussed and the results of the potential flow analysis.

The simple augmentation technique has the smallest effect on the theoretical two-dimensional lift curve slope; the Etkin techniques each have more pronounced three-dimensional effects, further decreasing the predicted value of C_{L_α}. This is to be expected given that the simple augmentation theory only takes into account the aspect ratio of the wing, neglecting possible influences from the wing geometry and compressibility effects. Figure 3.4 shows the MAPIR pod lift curves using the results from potential flow theory and the three wing theory predictions.

Table 3.1 – Summary of MAPIR Pod C_{L_α} and Lift Curve Equations Using Various Wing Theory Techniques and Potential Flow Results

	Simple Augmentation	Etkin Graphical	Etkin Semi-Empirical
C_{L_α} (deg^{-1})	0.02012	0.01219	0.01609
Lift Curve Equation	$-2.3986 + 0.02012\alpha$	$-2.3986 + 0.01219\alpha$	$-2.3986 + 0.01609\alpha$

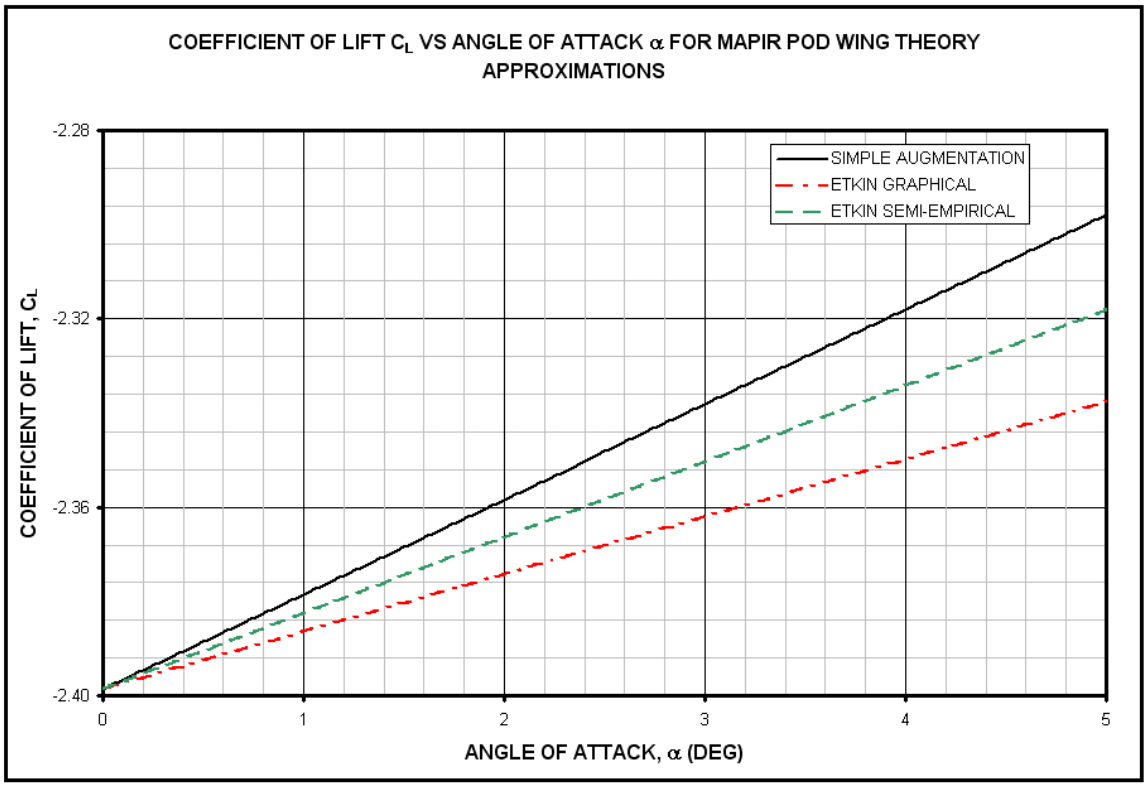

Figure 3.4 – Coefficient of Lift C_L vs. Angle of Attack α
for MAPIR Pod Wing Theory Approximations

Once again it is important to reiterate the driving assumption for choosing to use wing theory to analyze the MAPIR Pod. The geometry of MAPIR Pod cross-section loosely resembles that of a negatively-cambered airfoil, and thus the pod was considered to act like a wing with a very low aspect ratio. However, the MAPIR Pod is positioned on the aircraft fuselage and thus has flow over only its bottom and sides, as opposed to an actual wing that experiences flow over *all* its surfaces. This discrepancy had to be deliberately ignored for the preceding analysis.

CHAPTER IV
DRAG PREDICTIONS

As discussed regarding potential flow theory, drag is a viscous phenomenon. Such effects are confined to a relatively thin boundary layer near the body surface in high Reynolds number flows, and to regions where the geometry or pressure gradient causes flow separation; this type of drag is known as parasite, or zero-lift, drag. (Raymer, 327) A second type of drag, induced drag, results from lifting surfaces; such drag is typically proportional to the square of the lift generated. The total drag is then a sum of these values:

$$C_D = C_{D_0} + C_{D_i} \tag{4.1}$$

Skin friction drag results from the viscous effects within the boundary layer generated by attached flows. At low Reynolds numbers the flow over a body is laminar, yielding a skin friction coefficient of:

$$C_{d_f} = \frac{1.328}{\sqrt{\mathrm{Re}}} \tag{4.2}$$

At Reynolds numbers above approximately $5x10^5$, laminar flow will transition to turbulent. Turbulent flows are inherently random in nature; this randomness requires curve-fit approximations for turbulent flow effects. For the skin friction generated by turbulent flow over a flat plate, Raymer gives the semi-empirical formula (Raymer, 329):

$$C_{d_f} = \frac{0.455}{\left(\log_{10}\mathrm{Re}\right)^{2.58}\left(1+0.144M^2\right)^{0.65}} \tag{4.3}$$

It is important to note that the reference areas for the coefficients in both equations 4.2 and 4.3 are based on a surface's wetted area, or the area that is in contact with the flow.

While most aircraft experience both laminar and turbulent flow, it is assumed that the MAPIR Pod only encounters turbulent flow. As discussed in regards to wing theory for the pod, the aircraft fuselage upstream of the MAPIR pod energizes the boundary layer before the flow reaches the leading edge of the pod. Once again, using 130 mph as an average airspeed, the MAPIR Pod Reynolds number was found to be:

$$\mathrm{Re}_{avg} = \frac{\left(L_{fuselage} + C_{pod}\right)V}{\nu} = 2.158\times10^7$$

At 130 mph and sea level conditions, the Mach number is:

$$M = \frac{(130\text{ mph})(1.4667\text{ fps/mph})}{(1116\text{ fps})} = 0.1709$$

Equation 4.3 then yields a turbulent skin friction coefficient of:

$$C_{d_f} = \frac{0.455}{\left(\log_{10}\mathrm{Re}\right)^{2.58}\left(1+0.144M^2\right)^{0.65}}$$

$$= \frac{0.455}{\left(\log_{10}2.158\times10^7\right)^{2.58}\left(1+0.144(0.1709)^2\right)^{0.65}}$$

$$= 0.002656$$

To find the pod's zero-lift drag coefficient C_{D_0}, this result must be scaled by the ratio of the pod's wetted area to its reference area:

$$C_{D_0} = \frac{S_{wet}}{S_{pod_{theory}}} C_{d_f} \tag{4.4}$$

Once again, this analysis assumes the pod does not have tapered forward and aft sections. Equation 4.4 then yields a MAPIR Pod C_{D_0} of:

$$C_{D_0} = \frac{S_{wet}}{S_{pod_{theory}}} C_{d_f} = \frac{\left(44.3531 \text{ ft}^2\right)}{\left(26.1284 \text{ ft}^2\right)}\left(0.002656\right) = 0.004509$$

One should note that this analysis assumes attached flow over all the MAPIR Pod surfaces; thus, the separation likely to occur on the aft cylindrical section of the pod discussed previously must be neglected.

The total drag resulting from bodies in contact is usually greater than the sum of the individual drag of those bodies in free-stream conditions; this effect is called interference drag, and can be very difficult to predict. Thus, historical results are often used in situations that require predicting the drag of interfering bodies.

Figure 4.1 shows data compiled by Hoerner for shapes similar to the MAPIR Pod. (Hoerner, 8-4) It is important to note that Hoerner's data uses the frontal area of a shape as the reference area for his drag coefficients. For the MAPIR Pod, figure 4.1 yields a drag coefficient between:

$$C_{D_{\bullet}} = 0.0567 \quad \text{and} \quad C_{D_{\bullet}} = 0.0633$$

As with the skin friction prediction, this prediction must be scaled by the pod's reference area, yielding:

$$C_{D_0} = \frac{S_{front}}{S_{pod_{theory}}} C_{D_{\bullet_{Hoerner}}} = \frac{3.855 \text{ ft}^2}{26.1284 \text{ ft}^2} = 0.1475 C_{D_{\bullet}}$$

$$\therefore C_{D_0} = 0.008363 - 0.009337$$

These values, as expected, are greater than that predicted using solely skin friction theory, which does not incorporate interference effects. Unlike the skin friction prediction, the Hoerner data does not exclude separated flow in its analysis.

Lift-induced drag, as mentioned, is a function of the square of the lift produced by a body, as well as the body's aspect ratio and how the lift is distributed over the geometry:

$$C_{D_i} = \frac{C_L^{\ 2}}{\pi A e} \tag{4.5}$$

The Oswald span efficiency factor *e* of the body acts to effectively reduce the apparent aspect ratio of the shape. *e* = 1 for lifting surfaces with the ideal parabolic lift distribution. However, few lifting bodies have this parabolic profile, and thus *e* < 1; for a typical aircraft the span efficiency is somewhere between 0.7 and 0.85. (Raymer, 347) The span efficiency of the MAPIR Pod is unknown, though likely very low; this is because the pod is not a true airfoil or wing.

Because different techniques predict varying values for both C_L and C_{D_0} for the MAPIR Pod, equation 4.1 cannot be tied to a single formulation. Rather, it must incorporate the results from whichever combination of lift and drag techniques is chosen.

Table 4.1 summarizes the possible values for the pod's parasite and induced drag, depending on predictive technique chosen.

Once again the assumptions used for the preceding analysis need to be restated. The flow over the pod was assumed to be turbulent everywhere, resulting from the length of fuselage upstream of the MAPIR Pod leading edge. The resulting Reynolds number was then used to determine the flat-plate skin friction coefficient, and thus the zero-lift drag coefficient, for the pod. This coefficient assumed fully attached flow for the length of the MAPIR Pod, which is unlikely do to the downstream geometry of the body. Furthermore, again the pod was treated as a low aspect ratio wing so that the induced drag could be predicted using traditional lifting-body theories.

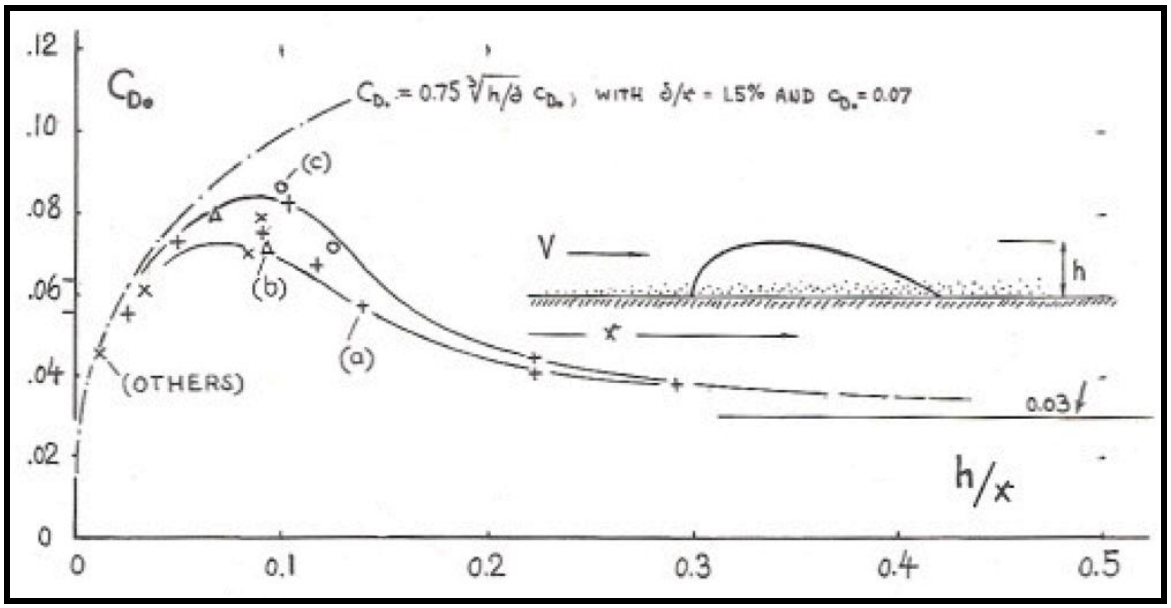

Figure 4.1 - Interference Drag Coefficient for Rounded Tapered Bodies

Table 4.1 – Summary of MAPIR Pod Parasite and Induced Drag Values for Various Predictive Techniques			
	Skin Friction	Hoerner Min	Hoerner Max
C_{D_0}	0.004509	0.008363	0.009337
	Simple Augmentation	Etkin Graphical	Etkin Semi-Empirical
C_{D_i}	$\frac{(-2.3986+.02012\alpha)^2}{\pi(0.4494)e}$	$\frac{(-2.3986+.01219\alpha)^2}{\pi(0.4494)e}$	$\frac{(-2.3986+.01609\alpha)^2}{\pi(0.4494)e}$

CHAPTER V
CFD ANALYSIS PREDICTIONS

Computational fluid dynamics (CFD) analysis gives engineers powerful tools for approximating the effects of complex flows over intricate geometries. The Navier-Stokes equations that govern fluid dynamics are highly non-linear, coupled partial differential equations; they can only be solved analytically for basic geometries and simplified – and therefore often *unrealistic* – flows. CFD techniques, on the other hand, rely on numerical methods to find approximate solutions to the Navier-Stokes equations; CFD analysis therefore is not limited by geometric or flow properties.

As with any approximation, the greater the accuracy required in the solution, the more difficult reaching that solution becomes. The code complexity, computer processing power required to evaluate the solution, and the time necessary to solve a given problem all increase with increasing complexity of the problem being evaluated. Furthermore, the validity of a CFD method must be verified before it can be used for predicting flows. The results from these computational techniques are also susceptible to human errors in both the problem design and the interpretation of the results.

Many different approaches exist for solving the equations of fluid motion; determining which method is appropriate depends on the nature of a given flow problem, the resources of those investigating the problem, and the accuracy desired in the solution. Unsteady flows involving viscous phenomena, such as vortex-shedding and flow separation, or involving compressibility effects, such as shockwaves at transonic and supersonic speeds, present a much greater challenge to accurately model than steady, low-speed flows over simple, streamlined geometries.

Semiempirical CFD methods combine experimentally-collected data with theoretical models to find low-fidelity, preliminary solutions to design problems. (Bertin, 549) These techniques augment highly simplified Navier-Stokes equations with experimental data, yielding faster but lower-fidelity results than other more advanced CFD methods.

Discretized flow models convert the Navier-Stokes equations from continuous, partial differential equations into discrete, algebraic equations that can be solved iteratively. Such methods can require vast computational power, so techniques to simplify their application have been developed. Two-layer flow models employ theories governing high Reynolds number flows, breaking a region into a thin, viscous boundary layer near surfaces and an inviscid region everywhere else. (Bertin, 551) While the complete discretized Navier-Stokes equations must be solved within the boundary layer, this region is small compared to the entire computational domain, which is dominated by inviscid flow that, as discussed regarding potential flow theory, is far simpler to solve.

Adaptive meshing is another way to improve cumbersome discretized CFD methods; in this process, the flow field mesh in which the equations of motion are solved is altered to optimize speed and accuracy during computation. (Bertin, 521) Adaptive meshing analyzes the flow field during calculation and finds regions with low- and high-flow gradients. In regions of low gradients, adjacent cells in the mesh are merged, decreasing the number of cells in that area, thus speeding up calculation. In regions of

high gradients, cells are split, increasing the number of cells and thus improving the accuracy in these more complex flow regions.

The MAPIR Pod analysis was done using a commercially available CFD program, SolidWorks Flow Simulation. This program, like many similar software packages, requires the user to simply define the problem geometry and initial flow conditions; no coding of algorithms or discretization of the Navier-Stokes equations is necessary to execute a simulation. The SolidWorks Flow Simulation software uses a finite-volume approach to solving the equations of motion, which are discretized in a conservative form (this entails including the conservation of mass equation when discretizing the Navier-Stokes equations, eliminating a common source of error in computational solutions.) Furthermore, the SolidWorks Flow Simulation software utilizes adaptive meshing to hasten solutions to flow problems. (SolidWorks, 1-31)

As mentioned, the geometry on which CFD techniques are used affects the speed of computation; when only limited computational power is available, complex geometries are often simplified and large flow regions contracted to yield faster, though less accurate, results. The extent of such simplifications must be carefully considered, for the simulation will yield results whether it is given an accurate approximation or a meaningless simplification.

The CFD analysis of the MAPIR Pod required such a geometric simplification. Beyond the limitations imposed by the available computing power (see Appendix A2 for computer specifications), no accurate digital model of all or part of the aircraft existed. Simply modeling the aircraft would have been highly time consuming, and including some or all of such a model in the flow simulation would have further lengthened the time required to find results. Thus, as with the potential flow and drag analysis for the pod, the fuselage of the aircraft was approximated by a flat plate surrounding the MAPIR Pod.

The simulation's simplified flat-plate geometry was assumed to be valid for a number of reasons. In the areas immediately forward and to the sides of the pod the fuselage and wings did not drastically change geometries. Aft of the pod the fuselage did sweep upward (as seen in figure 1.2), but the flow in this region without the pod installed was known to be attached. Furthermore, the MAPIR Pod was installed on the centerline of the aircraft, centered between the propeller washes. Thus, it was assumed that a flat-plate approximation would yield acceptable results. Figure 5.1 illustrates the geometry of the pod OML used in the simulation, as well as the size of the computational domain in which the analysis was run.

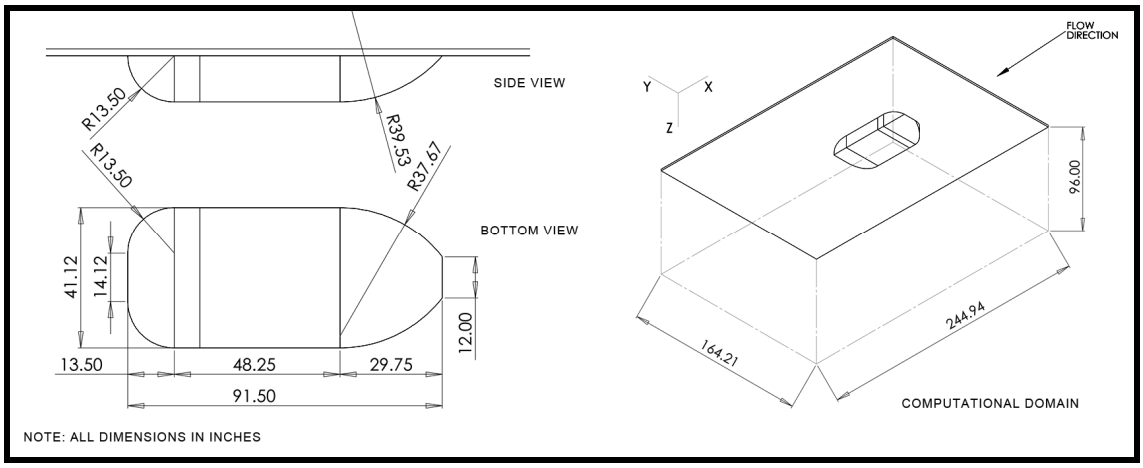

Figure 5.1 – CFD Analysis Geometry

To find a meaningful lift and drag polar, the simulation needed to be executed at a range of airspeeds and angles of attack. Thus, a speed range of 75 mph to 250 mph, in 25-mph increments, was chosen at angles of attack ranging from 0 degrees to 10 degrees, in 2-degree increments. The stall speed (V_{stall}) of the aircraft is 81 mph and the never-exceed speed (V_{ne}) is 272 mph; thus, the simulation covered almost the entire operational envelope of the aircraft, $0.9V_{stall}$ to $0.9V_{ne}$. Standard sea level conditions of 59 degrees Fahrenheit and 0.002377 slugs/ft^3 were chosen for the flow temperature and density, respectively. Because the lift and drag polars calculated from the simulations are non-dimensionalized by the dynamic pressure, this decision was arbitrary. However, if the actual magnitudes of the forces experienced by the pod were desired, choosing sea-level conditions would present a worst-case scenario for dynamic pressures.

These simulations thus were run until the forces acting on the MAPIR Pod converged. Figure 5.2 illustrates this, showing a plot of the total force as a function of the analysis iteration for one simulation case. It can be seen that the force calculated converges within about 2000 iterations; however, no static value is ever reached. This is because the OML is not truly streamlined, and the simulation is predicting the shedding of vortices from the aft surfaces; as these vortices are shed, the lift and drag generated by the MAPIR Pod fluctuate. These fluctuations are rather regular in both amplitude and period, and thus an average force can easily be determined for a given simulation case. The number of iterations it took each case to converge varied, though all the cases were run for over 3,000 iterations and some as many as 15,000.

SolidWorks Flow Simulation outputs forces in the body axis system as defined within the simulation; for analysis of the MAPIR Pod, the body coordinate system was defined in the traditional aircraft manner, with the x-axis pointing forward, the y-axis pointing right, and the z-axis pointing down. To find the body's lift and drag, these forces must undergo a coordinate transformation to convert them to the wind axis system; this is achieved with an Euler transformation, shown by equation 5.1.

$$\begin{bmatrix} D \\ Y \\ L \end{bmatrix} = \begin{bmatrix} -\cos\alpha\cos\beta & -\cos\beta & -\sin\alpha\cos\beta \\ \cos\alpha\sin\beta & \cos\alpha\cos\beta & \sin\alpha\sin\beta \\ \sin\alpha & 0 & -\cos\alpha \end{bmatrix} \begin{bmatrix} F_x \\ F_y \\ F_z \end{bmatrix} \tag{5.1}$$

These forces can then be non-dimensionalized into values of C_L and C_D for the pod.

It is important to note that the reference area used for determination of the pod's lift and drag coefficients from the results of the CFD analysis is different than that used previously. As mentioned, the potential flow and drag analysis both neglected the curved profile of the forward and aft fairings; this allowed two-dimensional analysis to be employed and then expanded for a three-dimensional result. The reference area for these predictions was therefore simply the rectangular product of the pod chord and the pod span. On the other hand, the CFD analysis is a true three-dimensional prediction; as such, the true projected area of the OML is used, which is slightly less than the theoretical area.

$$S_{pod_{theory}} = b_{pod} c_{pod} = 26.1284 \text{ ft}^2 \qquad S_{pod_{true}} = 23.7658 \text{ ft}^2$$

Figure 5.3 shows the results from the CFD analysis of the MAPIR Pod OML for both C_L and C_D as a function of angle of attack α. As expected, the CFD analysis predicts suction forces, or negative lift coefficients, throughout the considered range of angles of attack. While wing theory predicted a linear increase in lift coefficient with angle of attack, the simulation shows a slight parabolic trend to the data. Instead of having the minimum lift coefficient (maximum suction) at zero angle of attack, Figure 5.3 shows that the CFD analysis predicts a minimum lift coefficient of -0.2618 at α = 3.28 degrees. At angles of attack greater than this, the data does follow the trend predicted by wing theory, with C_L increasing with increasing α.

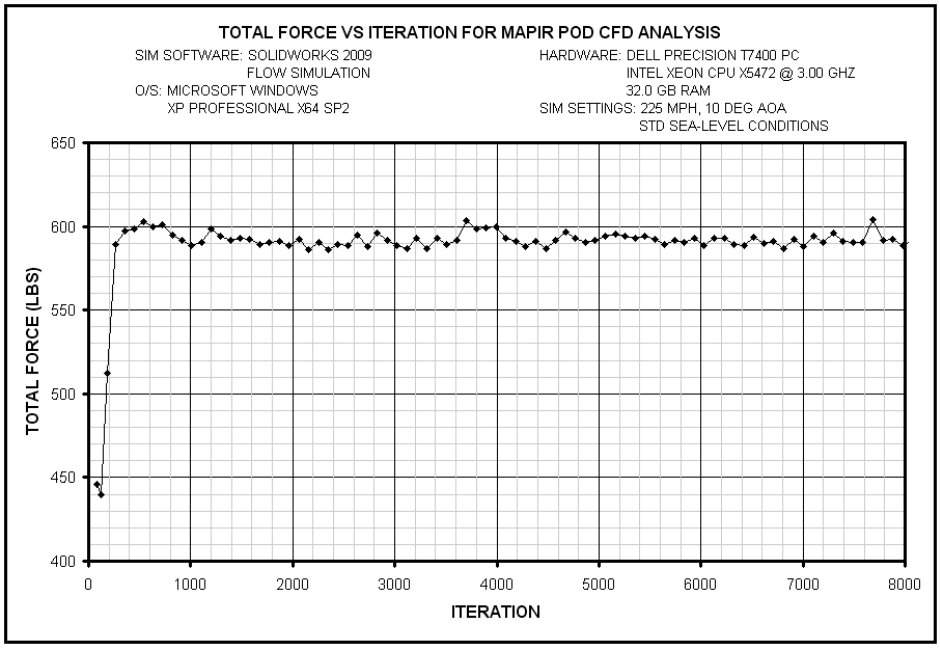

Figure 5.2 – Total Force vs. Iteration for MAPIR Pod CFD Analysis

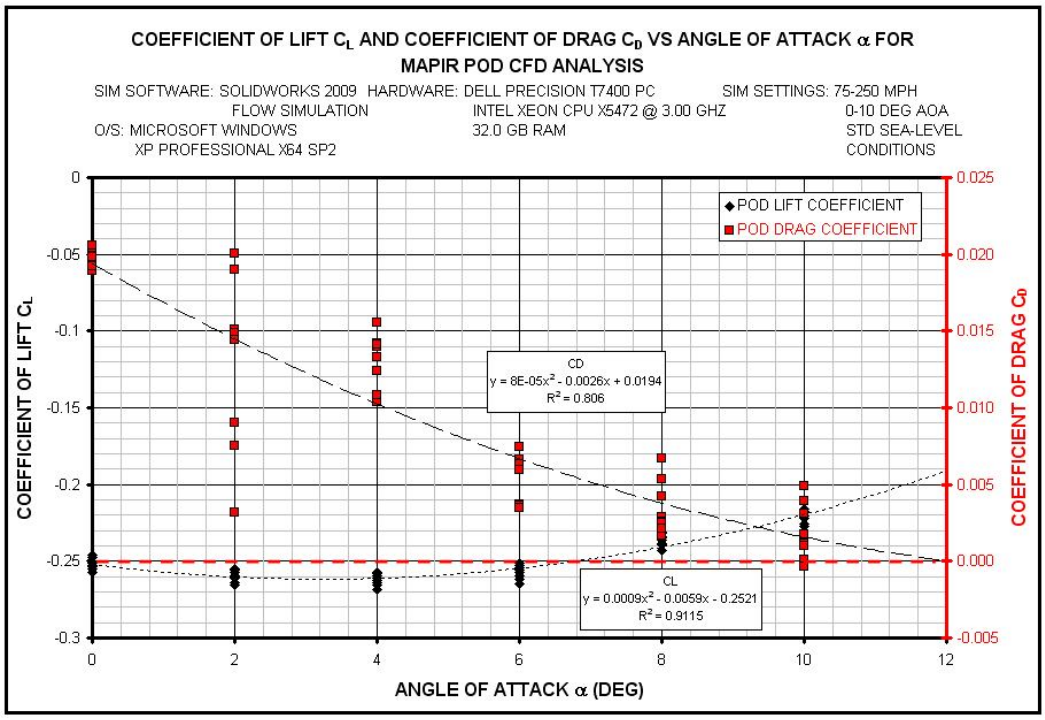

FIGURE 5.3 - Coefficient of Lift C_L and Coefficient of Drag C_D vs. Angle of Attack α for MAPIR Pod CFD Analysis

Figure 5.3 would also indicate that the CFD prediction for the pod's drag follows the trend established by the parasite and induced drag analysis conducted previously. As discussed, induced drag is a function of the *square* of the lift coefficient; thus, as the magnitude of C_L increases, so does the drag. Thus, as the magnitude of the lift coefficient decreases with increasing angle of attack, so to does the coefficient of drag.

Figure 5.4 illustrates the CFD results for the pod coefficient of lift as a function of the coefficient of drag. The data in the figure shows that the apparent confirmation of theory found from Figure 5.3 is in fact false. If the CFD predictions followed the lift and drag theories previously discussed, the trend in Figure 5.4 should be of the form $C_L = f\left(\pm\sqrt{C_D}\right)$. However, it can clearly be seen that the CFD analysis predicts a parabolic trend of the form $C_L = f\left(C_D{}^2\right)$. The magnitudes of the data predicted by CFD analysis are also drastically lower than those found using the potential flow, wing, and drag theories; these facts initially act to decrease the confidence in the CFD results. Without a truth source, however, determination of which prediction – or whether *any* of the predictions – is accurate is impossible; thus, flight testing of the aircraft was conducted to find the actual aerodynamic effect of the MAPIR Pod.

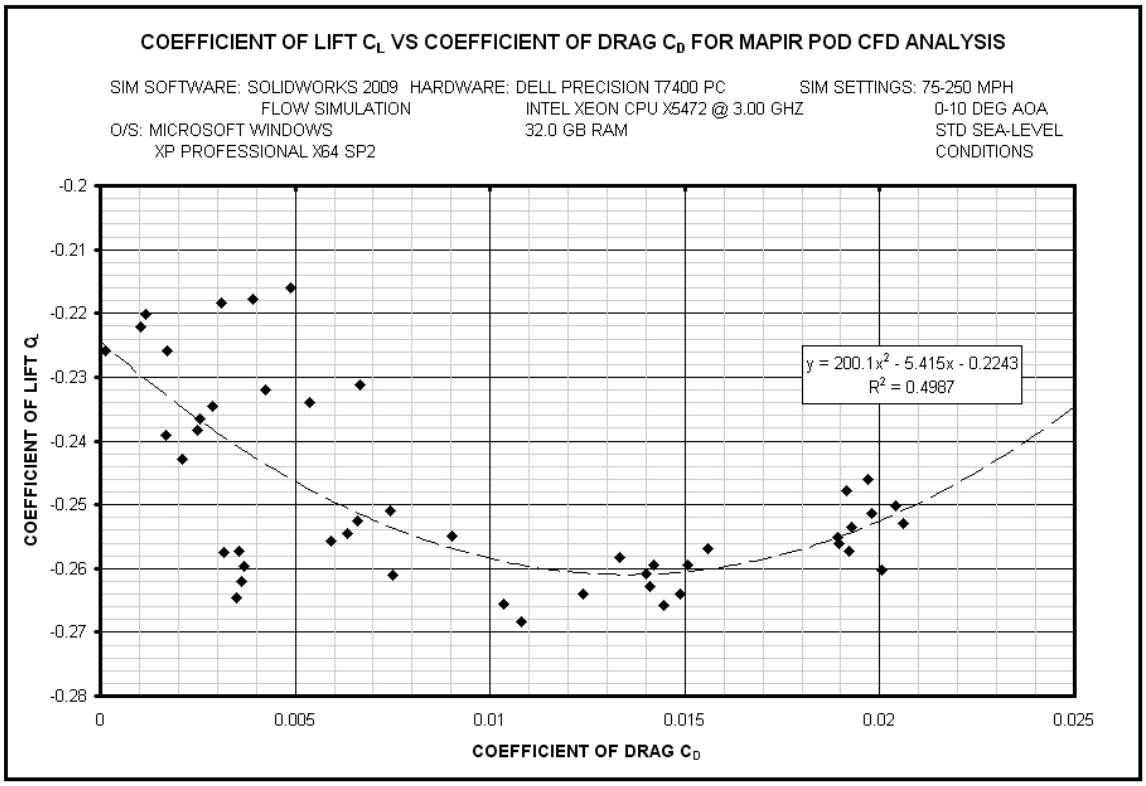

Figure 5.4 – Coefficient of Lift C_L vs. Coefficient of Drag C_D for MAPIR Pod CFD Analysis

CHAPTER VI
FLIGHT TESTING

Any aircraft that undergoes a modification to its OML requires flight testing to verify that the changes made do not impact the flight characteristics in an undesired or unexpected manner; such evaluation requires skilled personnel and a rigorous test regime to clear the operational flight envelope. However, flight testing can also be utilized to validate predictions made during the design process of the OML modifications. The conclusions from this type of analysis are not the performance changes but rather what those variations indicate for the OML changes enacted.

There exist a variety of methods for determining the coefficients of lift and drag for a given body added to an aircraft. Direct techniques require instrumentation, such as force transducers and load cells, to directly measure the loads experienced on the body during flight; such instrumentation is often very expensive and difficult to install. Furthermore, this type of specialized instrumentation is usually only applicable for testing the loads on the article of interest, and would serve little future purposes in the aircraft if it remained installed.

Indirect techniques for measuring force coefficients, however, require far less specialized or expensive instrumentation. Instead of directly determining the aerodynamic loads on a body, the forces are found from finding the *change* in flight characteristics from a baseline configuration to the modified configuration.

For a given force *f*, the aircraft force coefficient for a modified configuration $C_{f_{modified}}$ can be represented by the equation

$$C_{f_{modified}} = C_{f_{clean}} + \frac{S_{body}}{S_{A/C}} C_{f_{body}} \tag{6.1}$$

where $C_{f_{clean}}$ is the force coefficient of the aircraft in the baseline configuration, $C_{f_{body}}$ is the force coefficient for the added geometry, S_{body} is the reference area for the added geometry, and $S_{A/C}$ is the reference geometry for the aircraft in the baseline configuration. Both $C_{f_{clean}}$ and $C_{f_{modified}}$ use the baseline $S_{A/C}$ reference geometry. Equation 6.1 can then easily be rearranged for $C_{f_{body}}$, yielding

$$C_{f_{body}} = \frac{S_{A/C}}{S_{body}} \left[C_{f_{modified}} - C_{f_{clean}} \right] \tag{6.2}$$

Equation 6.2 can then be used with indirect flight testing techniques to find the desired force coefficient. The aircraft is flown in the baseline configuration to determine $C_{f_{clean}}$; changes are then made to the OML and the test regime is repeated in the modified configuration. Because the reference areas are both known values, the desired force coefficient can easily be determined.

One should note that indirect methods such as this are more useful for measuring large-scale aerodynamic phenomena. OML modifications that cause significant flow changes can be measured with lower-fidelity, more common instrumentation. As the aerodynamic effects decrease in magnitude, both the precision and accuracy of the

instrumentation required to yield meaningful results increase; at a certain point, it is actually less practical to use an indirect method than a direct method for determining the aerodynamic loads on an OML modification.

This type of indirect analysis is applicable to aircraft in either steady or accelerating flight, though steady flight testing is simpler and eliminates potential sources of error. Figure 6.1 illustrates the force balance of an aircraft in flight. This diagram assumes that the angle of the thrust vector relative to the pitch angle θ is negligible; for propeller aircraft this is usually a valid assumption.

In steady flight, the sum of the forces in figure 6.1 must be zero; this allows for the unknown forces – typically lift and drag – to be determined by directly measuring or calculating the other values in the figure. However, if the aircraft were accelerating the sum of the forces would be non-zero and the acceleration would therefore need to be quantified to determine the unknown forces. While this is possible with accelerometers, such as attitude and heading reference systems (AHRS), these instruments are expensive and accurately employing the resulting acceleration data unnecessarily complicates the analysis. It thus is far more practical to eliminate this variable altogether and conduct the analysis for steady flight only; the lift and drag polars of the MAPIR Pod were determined using this type of indirect analysis.

Any rigorous flight test regimen should include sensor and data system calibrations to ensure the accuracy of the flight test results. Data systems are prone to errors; quantifying these prior to testing therefore is essential. Calibrating the baseline aircraft configuration not only achieves this, but also allows for qualitative assessment of the effects generated by modification to the aircraft OML. A significant change in air data system calibrations between the baseline and modified configurations indicates that considerable aerodynamic effects may be resulting from the changed OML.

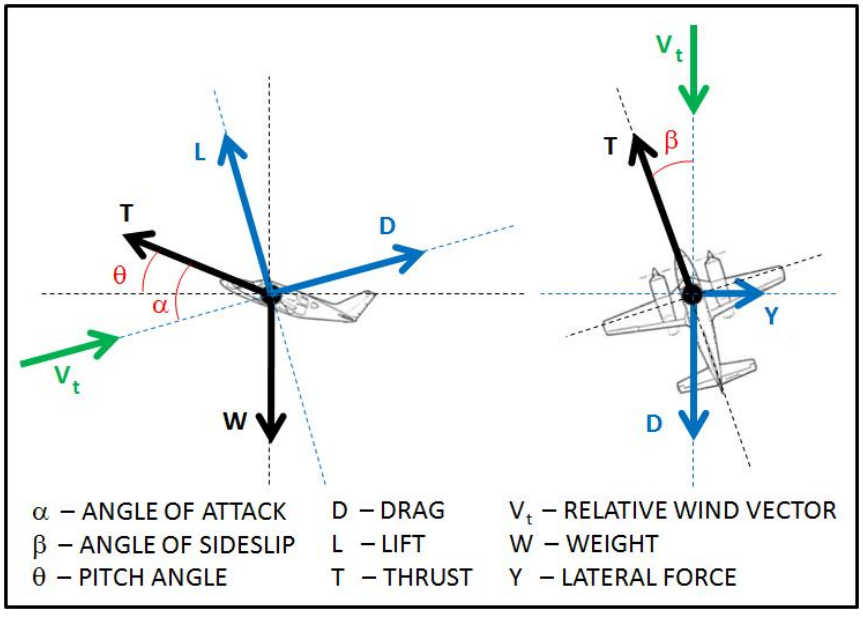

Figure 6.1 – Force Balance of Aircraft in Steady Flight

The MAPIR Pod flight test regime consisted of an angle of attack calibration, angle of sideslip calibration, airspeed calibration, and collecting steady, level data points at multiple airspeeds to determine the pod's lift and drag polars; this testing was executed for both the baseline and modified aircraft configurations.

The angle of attack calibration and the data point testing both required steady maneuvers at various airspeeds; their results thus were extracted from the airspeed calibration testing. Combining test techniques in this manner increases the efficiency of the flight test process; such consolidation opportunities are vital to missions with accelerated schedules, limited resources, and tight budgets.

A GPS four-course method (Lewis, 3) was used for the air data calibrations; such techniques are efficient and highly reliable when executed in stable air masses. (Kimberlin, 37) The airspeeds chosen for the calibrations ranged from 100 mph to 160 mph, in 20 mph increments; prior flight testing of the pod for handling and safety evaluation showed that these speeds could be easily maintained in steady flight with the pod installed.

Figures 6.2 and 6.3 show the altitude position error and velocity position errors as functions of indicated airspeed for both the baseline and modified aircraft configurations. While the magnitudes of the altitude and velocity errors for both configurations are small, there clearly exists a difference between the two calibrations. The calibration flights for each configuration were executed in very stable air masses, thus providing very reliable results. The air data system used for this test had both static and pitot ports located on the left nose of the test aircraft, far upstream of the MAPIR Pod; these factors tend to indicate that the variation in calibration curves for the two configurations is a qualitative indication that the MAPIR Pod had a measurable effect on the flow around the aircraft. Furthermore, this suggests that the flow effects are of a large enough scale that the indirect testing methods chosen were in fact applicable.

The angle of attack sensor was easily calibrated from the steady flight data collected during the air data system calibration. In steady, level flight, the angle of attack and the pitch attitude should be equal. Thus, plotting pitch attitude θ versus angle of attack α yields a calibration for the true angle of attack as a function of measured angle of attack. Figure 6.4 shows the results for the MAPIR Pod testing. The angle of attack calibration did not have a noticeable change between the modified OML and baseline configurations; this is surprising because the angle of attack indicator is located in the same position as the air data system probes, just on the opposite side of the aircraft. Thus, while the MAPIR Pod disrupted the pressure distribution in the region of the sensors enough to affect the air data readings, the flow direction was not significantly impacted.

No direct angle of attack instrumentation was installed on the MAPIR Pod; thus, an indirect method for measuring α for the pod had to be utilized. As with the aircraft, the angle of attack of the pod was assumed to be equal to its pitch angle during steady level flight. Because θ for the pod and θ for the aircraft were coincident, measuring the latter was therefore assumed to be the equivalent of measuring the former directly.

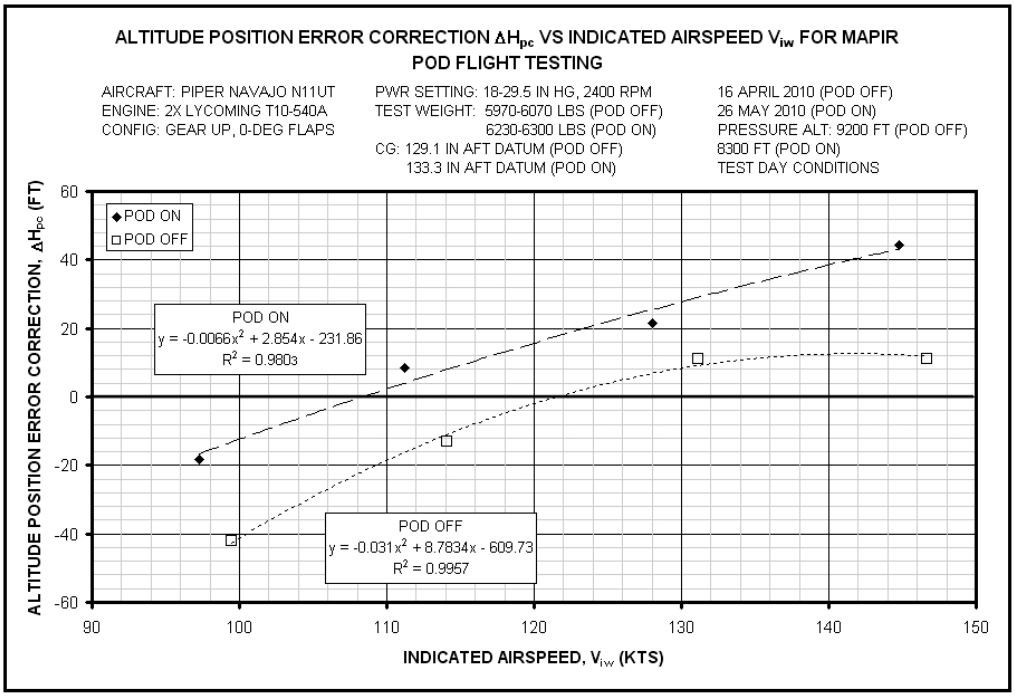

Figure 6.2 – Altitude Position Error Correction ΔH_{pc} vs. Indicated Airspeed V_{iw} for MAPIR Pod Flight Testing

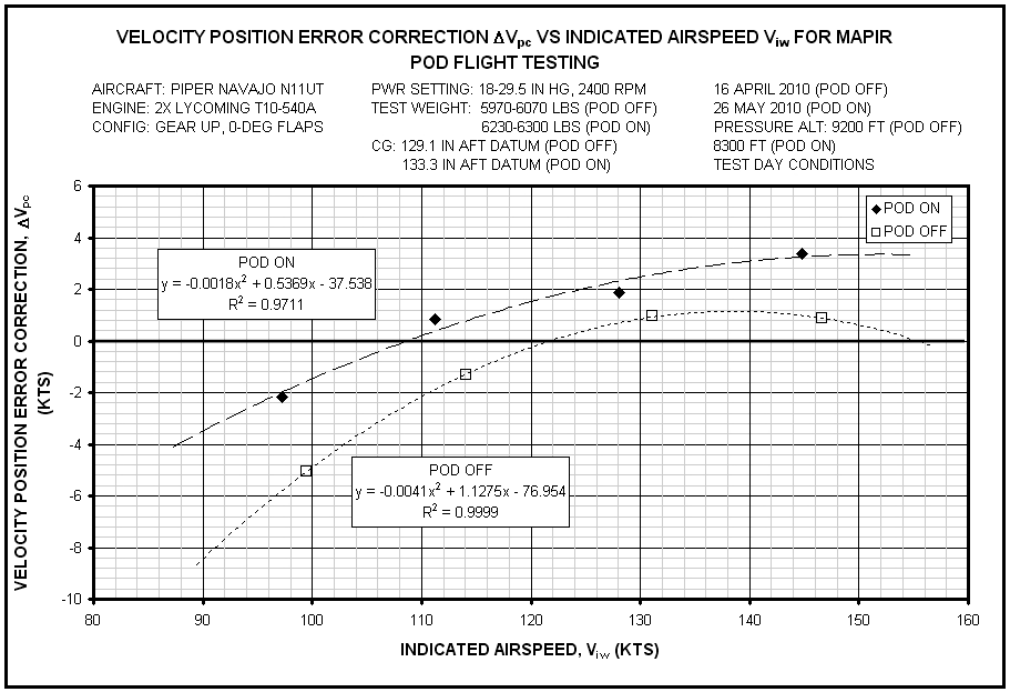

Figure 6.3 – Velocity Position Error Correction ΔV_{pc} vs. Indicated Airspeed V_{iw} for MAPIR Pod Flight Testing

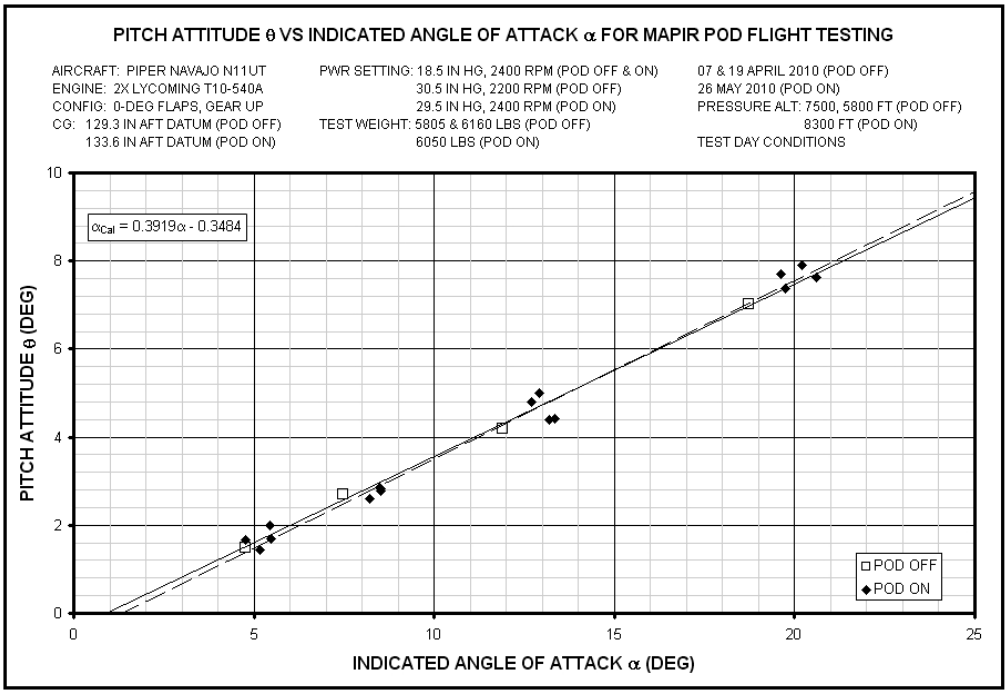

Figure 6.4 - Pitch Attitude θ vs. Indicated Angle of Attack α for MAPIR Pod Flight Testing

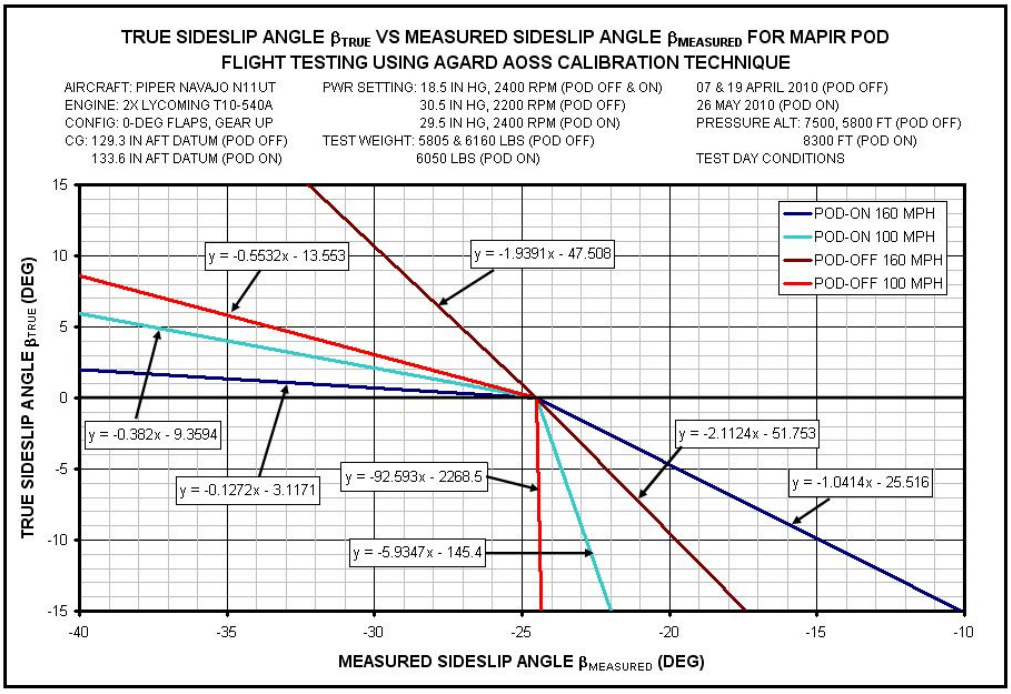

Figure 6.5 – True Sideslip Angle β_{true} vs. Measured Sideslip Angle $\beta_{measured}$ for MAPIR Pod Flight Testing Using AGARD AOSS Calibration Technique

An angle of sideslip calibration was also executed for both aircraft configurations; unlike the angle of attack and air data calibrations, the sideslip calibration required dynamic, flat turn maneuvers. (Lawford and Nippress, 51) Analytic and CFD predictions for the pod polars were only done at zero angle of sideslip; as such, the flight testing executed was also conducted at zero sideslip. Thus, the results from the sideslip calibration are only useful to ensure the testing did occur at negligible sideslips and for quantitative evaluation of the MAPIR Pod effects. A full discussion of the sideslip calibration theory and data reduction techniques can be found in Appendix A3.

Figure 6.5 shows the sideslip calibration curves for the baseline and modified aircraft configurations at low and high airspeeds. The nature of the sideslip sensors on the test aircraft, in conjunction with the propeller effects, contributes to the variation in calibration curves between left and right sideslips. The test aircraft had a primitive flush air data system for measuring sideslip; the system consisted of only two ports located on the sides of the radome. Unlike a boom with a sideslip vane, this type of configuration's calibration is dependent on airspeed; this effect can be seen in the differences in calibrations between the sideslips in the same direction and for the same configuration, but at different speeds. The drastic variations in calibrations from left to right sideslips likely results from propeller effects; the aircraft does not have counter-rotating propellers and the propellers are located quit close to the aircraft's nose. The flow disturbances thus are not symmetric, yielding the discrepancies in the calibration curves. Despite these factors, figure 6.5 once again qualitatively illustrates that the presence of the MAPIR Pod on the aircraft fuselage has a profound aerodynamic effect well upstream of the installation.

As discussed previously, the data points used to determine the aircraft lift and drag polars were collected from the steady, level air data calibration testing. Quantifying the lift and drag forces in figure 6.1 required measuring or calculating all the other variables in that figure at each test point. This was achieved using the aircraft's data acquisition system (DAS), which logged data at 20 Hz during the testing. The data stream was monitored in real time, with running averages and standard deviations of the data displayed. This allowed the flight test engineer (FTE) to determine whether a test point was valid or if it needed to be repeated depending on whether critical parameters stayed within pre-defined tolerances. Each test point was held for approximately 10 seconds; this was done so the data in the interval could be averaged, smoothing any random variations in the data (such as turbulence or sensor noise) that would skew a smaller sample size.

The test weights were determined by adding the fuel weight during the test maneuver to the empty aircraft weight, determined prior to flight testing, and crew weight; the fuel quantity could not be logged by the DAS, so these values were recorded by hand for each test point. The pitch angle θ was measured with the aircraft's AHRS; once again, in steady, level flight θ and the calibrated α were expected to be equal, and testing confirmed this. The aircraft was trimmed into the relative wind, so there was negligible sideslip during the test points.

Determining the magnitude of the engines' thrust was a more complex process. First, the horsepower generated by the engines had to be calculated using manufacturer-provided engine graphs for different RPM settings. To use these charts, the engine RPM,

manifold pressure, and inlet temperature had to be recorded, as well as the pressure altitude for the test point; an ideal horsepower could then be read from the graph and corrected for altitude temperature variations.

To speed the data reduction and ensure consistent interpolation of the graphical data, a software routine was developed in National Instruments' LabVIEW coding language to automate much of the process. The trend lines in the various horsepower graphs were carefully quantified; a routine then was written that interpolated the data for intermediate data points that fell between the displayed curves. The software further interpolated between graphs, allowing horsepower values to be calculated for RPM settings that did not correspond to one of the provided charts.

The horsepower values could then be used to determine the engines' thrust; this required determining the propeller efficiencies at each test point. A LabVIEW routine, developed by Joe Young, combined the calculated horsepower and other test point values with manufacturer-supplied propeller efficiency data to compute the thrust for each engine.

With all the known variables quantified in the force balance from figure 6.1, the lift and drag forces for the baseline and modified configurations were then solved and non-dimensionalized into C_L and C_D polars. Figure 6.6 shows both the coefficient of lift and coefficient of drag as a function of angle of attack for both configurations.

The linear trend for the lift coefficient and the parabolic trend for the drag coefficient are maintained between configurations. The addition of the pod to the aircraft OML has only a slight effect on the lift curve; surprisingly, the curve is raised slightly, indicating the addition of the pod actually increased the total lift of the aircraft despite analysis that predicted a decrease in lift due to suction. The modified configuration data does have more scatter at higher angles of attack than the baseline data, and could account for some of the data trend shift displayed in the figure.

The drag polar is also shifted by the addition of the MAPIR Pod. At higher angles of attack (which correspond to slower flight speeds), the modified configuration displayed slightly lower drag values. However, at low angles of attack (higher speeds), the addition of the pod tended to raise the total drag. Unlike the lift coefficient data, the drag coefficient data for the modified configuration had little scatter anywhere in the data set.

These trends are highlighted in figure 6.7, which shows the coefficient of drag C_D as a function of the coefficient of lift C_L for both the baseline and modified aircraft configurations. At low lift coefficients, where the pod-on data has low scatter, it can be seen that the presence of the MAPIR Pod definitely increases the total drag of the aircraft. The data collected at higher lift coefficients, however, has significantly more scatter; the modified configuration data could therefore potentially coincide much more with the baseline configuration points. The apparent shift in data trend between configurations therefore may be less indicative of an actual phenomenon and rather the product of errors in the flight testing.

This is unlikely, however, given the data displayed in figure 6.6. As discussed, only the lift coefficient data had increased scatter with the addition of the pod. Furthermore, the greatest change in C_L trend occurs in the region of lowest scatter, at low angles of attack. Combined with the cleanness of the C_D data in figure 6.6, the trends

shown in figure 6.7 are thus likely accurate representations of the actual effects of the MAPIR Pod on the test aircraft.

With equations for both the baseline and modified configuration lift and drag coefficients, equation 6.2 can be solved to yield formulas for the MAPIR Pod C_L and C_D. As with the analytic and CFD analysis, the aircraft angle of attack α will be used as the independent variable.

From figure 6.6, the baseline and modified coefficients are

$$C_{L_{clean}} = 0.0855\alpha + 0.2207 \qquad C_{L_{pod-on}} = 0.0833\alpha + 0.2435$$

$$C_{D_{clean}} = 0.0011\alpha^2 + 0.0003\alpha + 0.0329 \qquad C_{D_{pod-on}} = 0.0007\alpha^2 + 0.0018\alpha + 0.0361$$

For the pod lift coefficient, equation 6.2 then becomes

$$C_{L_{pod}} = \frac{\left(229\ \text{ft}^2\right)}{\left(23.766\ \text{ft}^2\right)}\left[\left(0.0833\alpha + 0.2435\right) - \left(0.0855\alpha + 0.2207\right)\right]$$

$$C_{L_{pod}} = 9.6356\left(-0.0022\alpha + 0.0228\right)$$

$$\therefore C_{L_{pod}} = -0.02120\alpha + 0.2197$$

Likewise, for the pod drag coefficient, equation 6.2 yields

$$C_{D_{pod}} = \frac{\left(229\ \text{ft}^2\right)}{\left(23.766\ \text{ft}^2\right)}[\left(0.0007\alpha^2 + 0.0018\alpha + 0.0361\right) - \left(0.0011\alpha^2 + 0.0003\alpha + 0.0329\right)]$$

$$C_{D_{pod}} = 9.6356\left(-0.0004\alpha^2 + 0.0015\alpha + 0.0032\right)$$

$$\therefore C_{D_{pod}} = -0.003854\alpha^2 + 0.01445\alpha + 0.03083$$

These formulations can now be used as truth sources for the pod aerodynamics to which the analytic and CFD predictions can be compared.

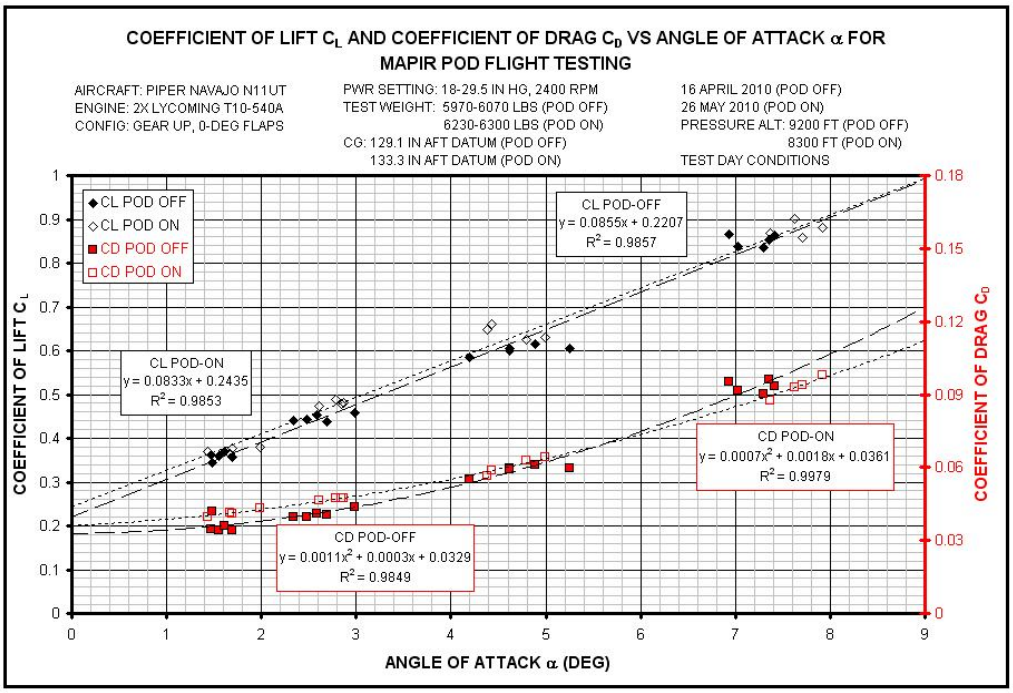

Figure 6.6 – Coefficient of Lift C_L and Coefficient of Drag C_D vs. Angle of Attack α for MAPIR Pod Flight Testing

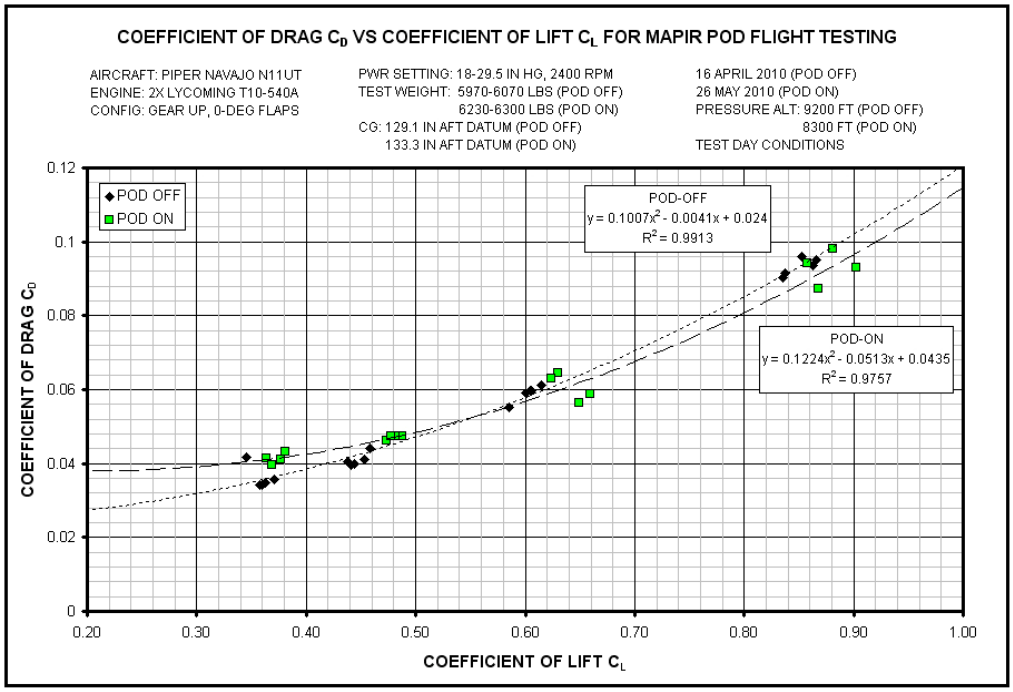

Figure 6.7 – Coefficient of Drag C_D vs. Coefficient of Lift C_L for MAPIR Pod Flight Testing

CHAPTER VII
RESULTS AND DISCUSSION

To validate the aerodynamic predictions for modification to an aircraft's OML, the predictions and the truth source data must be of the same format; this ensures that any comparisons made are both meaningful and instructive. The most common method to achieve this is through the use of non-dimensional coefficients; the indirect analysis methods previously discussed require the calculation of such coefficients, simplifying the validation process.

The analysis of the MAPIR Pod aerodynamics was executed with this consideration in mind; the trend-fitting for both the pod's lift and drag coefficients was done with respect to the pod's angle of attack; as discussed, this was equal to the angle of attack of the test aircraft. This ensured that a single dependent variable could be used to compare the results from the various predictive methods discussed with the experimental flight data. Furthermore, such a consistent format allows for other trends, such as lift-versus-drag polars, to be determined and analyzed.

Figure 7.1 shows the MAPIR Pod's coefficient of lift as a function of angle of attack based on the analytic and CFD predictions discussed in the previous sections, as well as the flight testing results. The analysis in Chapter III yielded three different lift curve slopes; however, these separate curves would overlap and thus be indiscernible if plotted at the scale set by figure 7.1. Thus, these results are combined into a single "analytic predictions" trend in the figure.

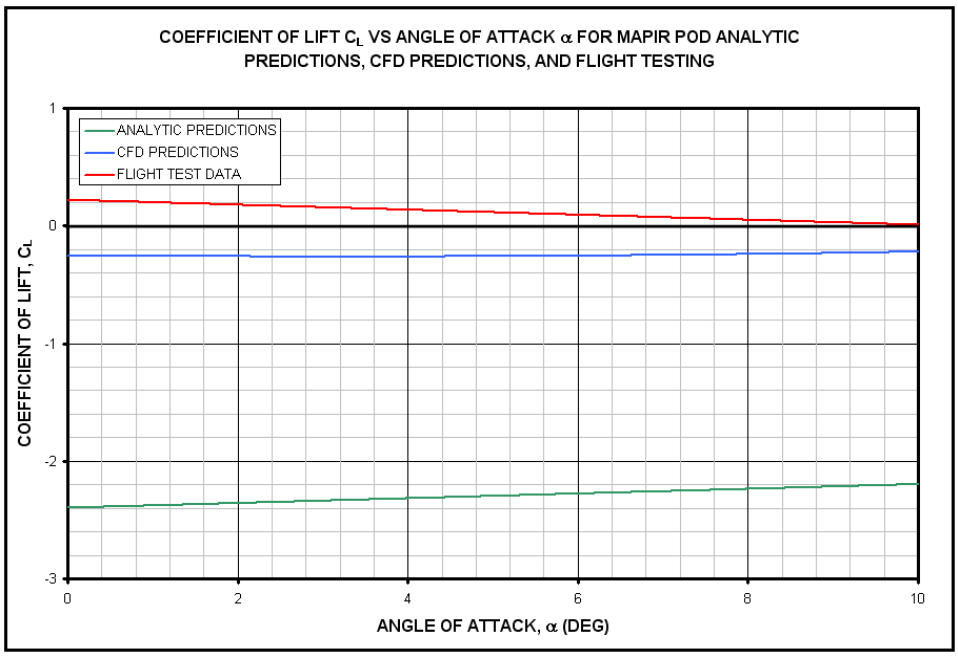

Figure 7.1 – Coefficient of Lift C_L vs. Angle of Attack α for MAPIR Pod Analytic Predictions, CFD Predictions, and Flight Testing

Figure 7.1 illustrates the vast discrepancy between the predictions and the actual aerodynamic properties of the pod. The wing theory predictions were the most erroneous, with the CFD analysis yielding slightly more accurate results. However, both of these methods predict negative pod lift coefficients that grow with increasing angles of attack; the empirical data, on the other hand, shows that the pod has a slightly *positive* lift coefficient that decreases with increasing α.

Figure 7.2 shows the MAPIR Pod's coefficient of drag as a function of angle of attack for the various predictive methods and for the empirical flight data. Unlike figure 7.1, figure 7.2 has multiple curves for the analytic predictions corresponding to the various span efficiencies chosen for the analysis. As the graph shows, increasing the span efficiency decreases the drag for a given angle of attack.

There exists a huge difference between the analytic drag predictions and those found from CFD analysis and from the flight data; the latter two curves appear almost coincident at the scale of figure 7.2. Furthermore, the magnitudes of the analytically-determined drag coefficients are far too high; this is thus an indication that the analytic drag analysis was faulty.

Figure 7.3 zooms in on the CFD and flight test data from figure 7.2, showing only the coefficient of drag found from CFD analysis and from flight testing as a function of angle of attack.

With the adjusted scale of figure 7.3, the overlapping trends of figure 7.2 radically diverge for the given angle of attacks. The CFD analysis shows a nearly linear decrease in drag with increasing α, whereas the experimental data follows a strong parabolic curve that initially increases to a maximum drag coefficient of 0.044 at an angle of attack of 1.9 degrees. The CFD analysis also underestimates the actual pod drag up to α = 4.9 degrees.

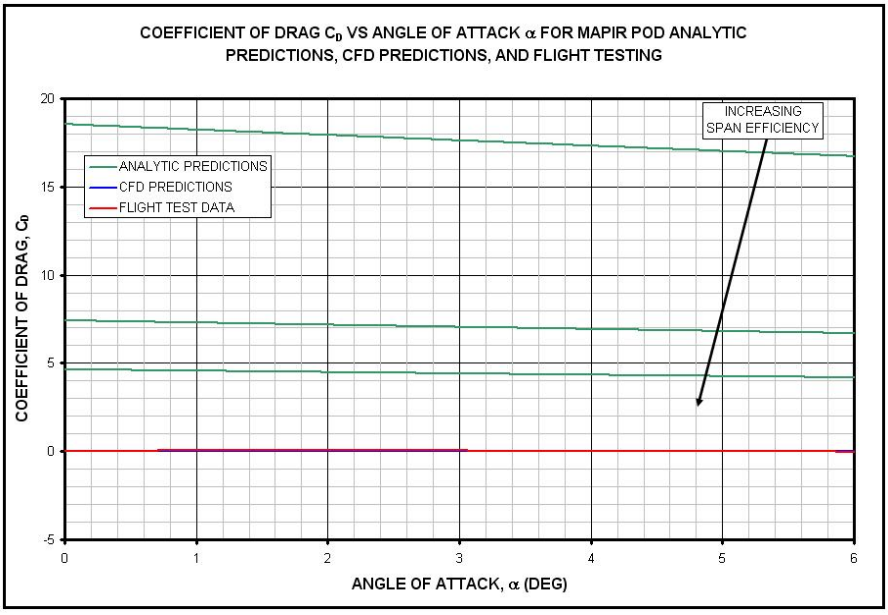

Figure 7.2 – Coefficient of Drag C_D vs. Angle of Attack α for MAPIR Pod Analytic Predictions, CFD Predictions, and Flight Testing

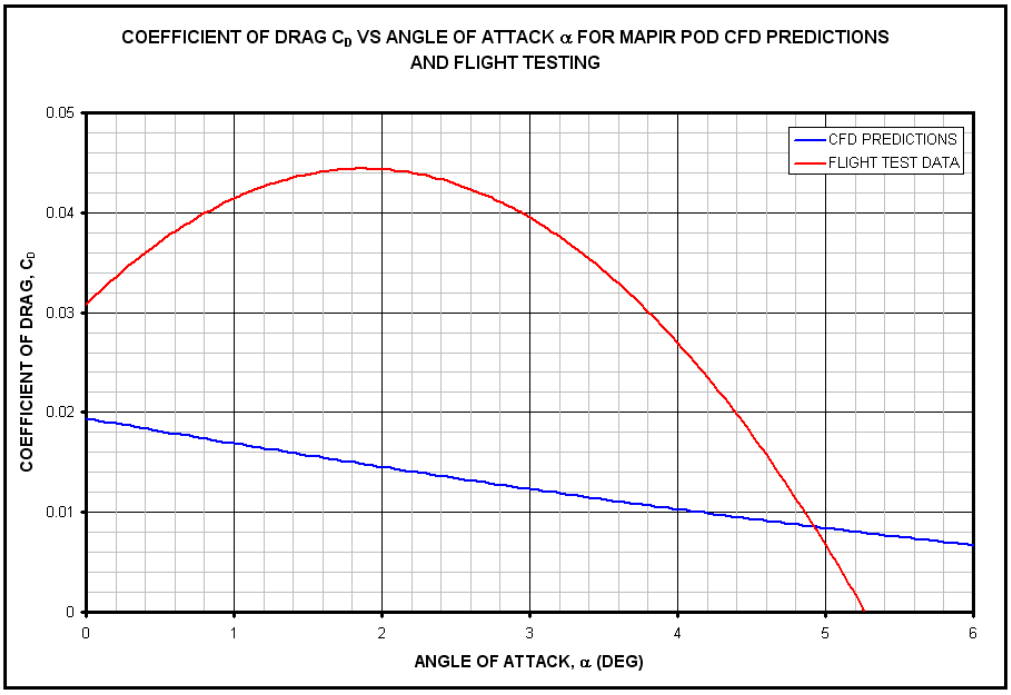

Figure 7.3 – Coefficient of Drag C_D vs. Angle of Attack α for MAPIR Pod CFD Predictions and Flight Testing

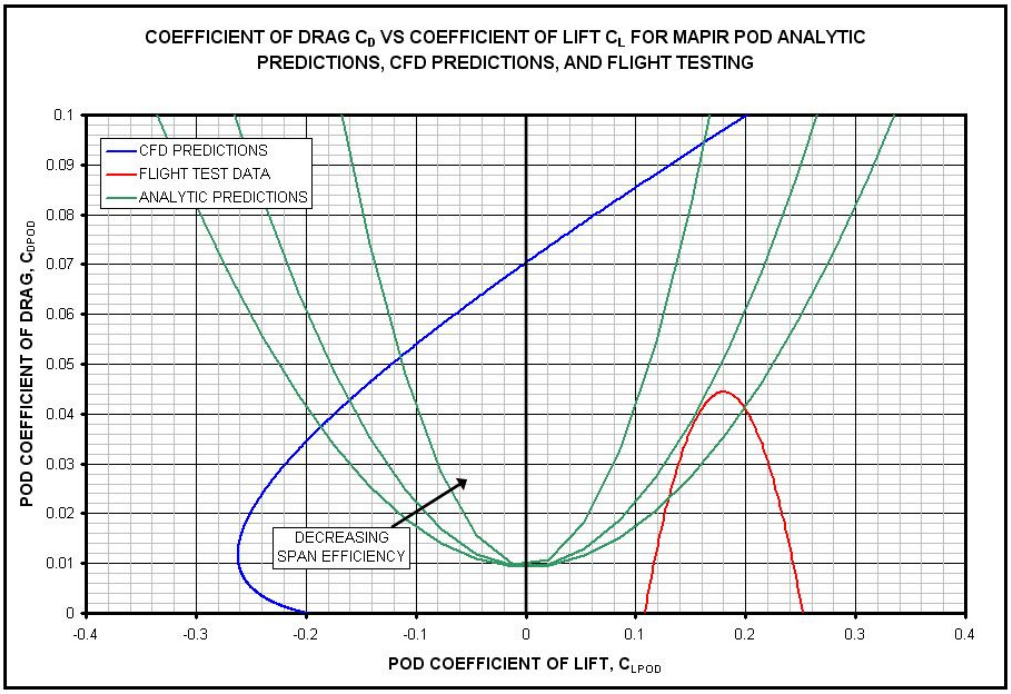

Figure 7.4 – Coefficient of Drag C_D vs. Coefficient of Lift C_L for MAPIR Pod Analytic Predictions, CFD Predictions, and Flight Testing

Having determined both C_L and C_D as a function of α for the pod, a drag polar for the various predictions and flight test data can be plotted. Figure 7.4 illustrates the pod coefficient of drag as a function of coefficient of lift for the analytic predictions, CFD analysis, and experimental flight test data.

Possibly more than any of the previous plots, figure 7.4 serves to highlight the drastic discrepancy between the results from the predictive methods and the actual aerodynamic characteristics of the MAPIR Pod when installed on the test aircraft.

This divergence between prediction and reality shows that the geometric and flow field assumptions made for the analytic and CFD analyses were overly simplistic. All these methods assumed steady flows at constant angles of attack; in actuality, the upstream aircraft bodies disrupted the flow field in ways that voided this assumption. As previously discussed, the test aircraft did not have counter-rotating propellers; this likely further contributed to disruptions in the flow field acting on the MAPIR Pod.

Furthermore, the geometric simplifications made for the predictions clearly were too profound to yield accurate results. In reality, the aircraft fuselage and wing geometries have a significant effect on the flow field in the vicinity of the MAPIR Pod installation. These geometries and the resulting flow effects, however, were neglected in all the predictive analyses. Potential flow theory treated the upstream and downstream aircraft fuselage as flat plates, neglected separation, and expanded two-dimensional analysis into three-dimensional predictions. Wing theory treated the MAPIR Pod like a finite wing experiencing free-stream flow over both an upper and lower surface; being affixed to the aircraft fuselage, only the pod's lower surface experienced flow, and this flow was disrupted from the upstream aircraft geometry. Similar to the analytic methods, CFD theory assumed that the fuselage of the aircraft could be approximated by an infinite flat plate; thus, the CFD analysis also failed to account for the complex flows arising from the aircraft geometry.

While the simplifications used for the MAPIR Pod analysis turned out to be erroneous, such assumptions are not necessarily flawed for all situations or all methods. The driving flaw in the MAPIR Pod analysis was that the pod was very large relative to the test aircraft; as such, the important assumption that the fuselage could be interpreted as a flat plate was not valid. Had flight testing occurred with a larger aircraft that more closely represented the predictions, the experimental results would likely have more closely matched the predictive analyses. Thus, the analytic and CFD techniques discussed are not inherently defective; however, the preceding discussion does highlight their limitations, at least with respect to the MAPIR Pod aerodynamic analysis.

CHAPTER VIII
RECOMMENDATIONS FOR FUTURE ANALYSIS

The predictive methods in the preceding discussion were all determined to be relatively invalid for the case of the MAPIR Pod, though not necessarily flawed for all situations. While this was the goal of the analysis, future investigations could be tailored to find what level of simplification can in fact be tolerated by the approximations and still yield accurate results. Furthermore, the flight testing methods executed could be improved to strengthen the confidence in the experimental data.

As discussed, a driving limitation in the analytic and CFD analysis was the geometric simplifications. The analytic predictions required these generalizations to allow the problems to be solved by hand; the CFD analysis, however, used these simplifications only to speed up the design and computational time. While no digital model existed of the test aircraft, it would not have been impossible to create a relatively accurate representation. However, the MAPIR mission requirements did not give the time to execute such a task, so the flat-plate approximation was used instead. If the MAPIR Pod analysis were to be revisited, implementation of such a digital model for the CFD analysis would likely yield much more accurate results. Furthermore, the amount of the aircraft included in the simulation could then be determined; simulations could be run with increasingly larger computational domains until the simulation results converged with the experimental flight test data.

Improvements in the flight testing regime would yield a better truth source as well. Scheduling and funding limited the amount of flight time available for this analysis; had more airspeeds been tested both inside and beyond the given dataset, the confidence in the data trends would be increased. The more data points present, the less impact an erroneous point has on the overall trends. Furthermore, upgrades in the instrumentation system – including a more accurate air data system and a better model of the engines' thrust – would improve the quality of the experimental data.

Repeating the flight testing on a larger aircraft could also improve the validity of some of the predictions. This would potentially act to make the flight conditions more accurately match the assumptions made for the predictions, thus improving those analyses' validities.

It is important to note, though, that the analysis undertaken was deliberately low-cost, high-speed, and executed with limited facilities so that budgetary and scheduling deadlines could be met. Many of the above mentioned improvements would be costly and time-consuming, thus violating these underlying driving considerations.

CHAPTER IX
CONCLUSION

It is essential when modifying an aircraft's OML to understand the aerodynamic effects such changes create; proper investigation of these properties inherently takes time and resources. However, accelerated schedules and tight budgets can mean that time is limited and resources are scarce; thus, assumptions must be made during the design process that can only be validated by experimentation.

For the case of the MAPIR Pod, simplifying assumptions were made so that potential flow theory, wing theory, and rapid CFD analysis could be employed to predict the pod's lift and drag properties in flight. Only after experimental flight testing was conducted was it shown that these simplifications were in fact too drastic, yielding invalid predictions.

The predictive methods discussed are thus impractical for use with the MAPIR Pod, but not inherently corrupt. The relative size of the pod with respect to the test aircraft was a driving factor in the failure of the predictions to match reality. However, had the MAPIR Pod been significantly smaller relative to the test aircraft, some of the predictive techniques likely would have been far more accurate.

The preceding analysis thus serves to highlight the challenges inherent in, and care that must be taken throughout, the design and testing of any complex aerodynamic system.

LIST OF REFERENCES

1. "Lycoming Aircraft Engine Performance Data – Engine Model T10-540A Series", Lycoming Engines, Williamsport, Pennsylvania.

2. *SolidWorks Flow Simulation 2009 Technical Reference*, Dassault Systèmes SolidWorks Corp, Concord, Massachusetts, 2009.

3. Abbott, I. H. and von Doenhoff, A. E., *Theory of Wing Sections Including a Summary of Airfoil Data*, Dover Publications, New York City, New York, 1959.

4. Ashley, H. and Landahl, M., *Aerodynamics of Wings and Bodies*, Dover Publications, Inc., New York City, New York, 1965.

5. Bertin, J. J., *Aerodynamics for Engineers, 4th Edition*, Prentice Hall, Upper Saddle River, New Jersey, 2002.

6. Etkin, B. and Reid, L. D., *Dynamics of Flight: Stability and Control, 3rd Edition*, John Wiley & Sons, Inc., New York City, New York, 1996.

7. Hoerner, S. F., *Fluid-Dynamic Drag: Practical Information on Aerodynamic Drag and Hydrodynamic Resistance*, Hoerner, Midland Park, New Jersey, 1958.

8. Kimberlin, R., *Flight Testing of Fixed Wing Aircraft,* AIAA, Reston, Virginia, 2003.

9. Lawford, J. and Nippress, K., *AGARD Flight Test Techniques Series, Volume 1: Calibration of Air-Data Systems and Flow Direction Sensors*, NATO, 1984.

10. Lewis, G., "Using GPS to Determine Pitot-Static Errors," National Test Pilot School, Mojave, California, 2003.

11. Panton, R. L, *Incompressible Flow, 3rd Edition*, John Wiley & Sons, New York City, New York, 2005.

12. Raymer, D. P., *Aircraft Design: A Conceptual Approach, 4th Edition*, AIAA, Reston, VA, 2006.

13. Ward, D. T. and Strganac, T. W., *Introduction to Flight Test Engineering, Second Edition*, Kendall/Hunt Publishing Company, Dubuque, Iowa, 1996.

14. Yechout, T. R., *Introduction to Aircraft Flight Mechanics*, AIAA, Reston, Virginia, 2003.

15. Young, J. K., *Untitled*, Masters Dissertation, Aviation Systems and Flight Research Dept., University of Tennessee Space Institute, Tullahoma, TN (to be published).

APPENDICES

APPENDIX A1
DERIVATION OF POD LIFT COEFFICIENT
USING IDEAL FLOW THEORY

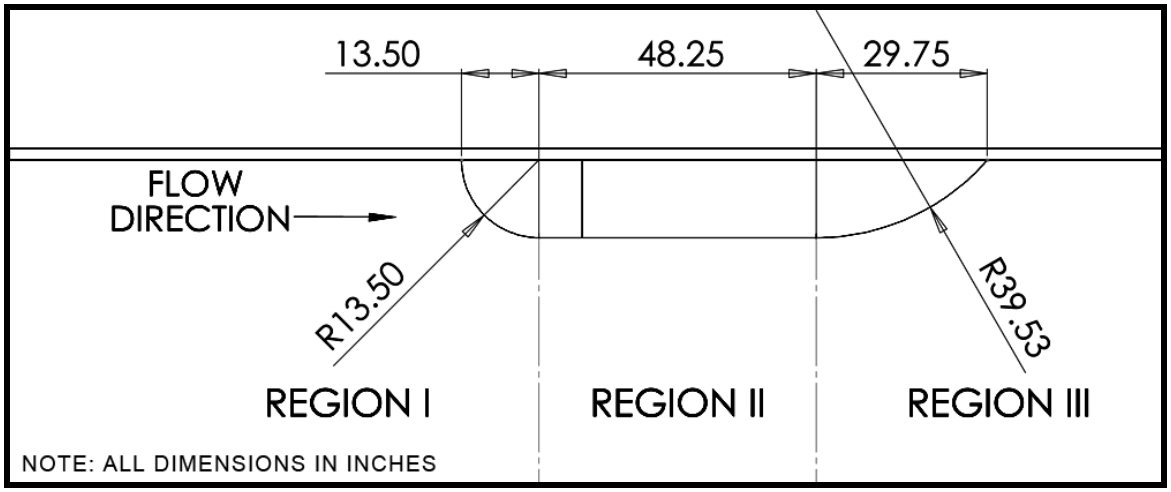

Figure A1.1 – Side Profile of MAPIR Pod for Potential Flow Analysis

The radial and tangential components of the two-dimensional velocity field over a cylinder (Panton, 423) are given by:

$$v_r = U\left(1-\frac{r_0^2}{r^2}\right)\cos\theta \qquad v_\theta = -U\left(1+\frac{r_0^2}{r^2}\right)\sin\theta$$

At the cylinder surface,

$$v_r = 0 \qquad v_\theta = -2U\sin\theta$$

This gives a two-dimensional pressure coefficient of:

$$C_{p_{circ}} = \frac{p-p_\infty}{\frac{1}{2}\rho U^2} = 1-4\sin^2\theta$$

The pressure coefficient in the lift direction (positive y-direction) is then:

$$C_{p_y} = C_p\left(-\sin\theta\right) = -\sin\theta+4\sin^3\theta$$

This is then integrated along the cylinder profile:

$$C_{L_{2D}} = \int\left(-\sin\theta+4\sin^3\theta\right)r d\theta$$

For Region I:

$$C_{L_{2D_{fwd}}} = \int_{\pi}^{3\pi/2}\left(-\sin\theta+4\sin^3\theta\right)r_{fwd}\,d\theta$$

$$C_{L_{2D_{fwd}}} = r_{fwd}\left(\left[\cos\theta\right]_{\pi}^{3\pi/2}+4\left[\frac{-3\cos\theta}{4}+\frac{\cos 3\theta}{12}\right]_{\pi}^{3\pi/2}\right)$$

$$C_{L_{2D_{fwd}}} = r_{fwd}\left(\left(0+1\right)+4\left[-\frac{3}{4}\left(0+1\right)+\frac{1}{12}\left(0+1\right)\right]\right)$$

$$C_{L_{2D_{fwd}}} = r_{fwd}\left(1-3+\frac{1}{3}\right) = -\frac{5}{3}r_{fwd} = -\frac{5}{3}\left(13.5\text{ in}\right) = -22.5\text{ in} = -1.875\text{ ft}$$

$$\therefore \frac{C_{L_{2D_{fwd}}}}{\text{ft}} = -1.875$$

For Region III:

$$C_{L_{2D_{aft}}} = \int_{3\pi/2}^{0.2288\pi}\left(-\sin\theta + 4\sin^3\theta\right)r_{aft}\,d\theta$$

$$C_{L_{2D_{aft}}} = r_{aft}\left(\left[\cos\theta\right]_{3\pi/2}^{0.2288\pi} + 4\left[\frac{-3\cos\theta}{4}+\frac{\cos 3\theta}{12}\right]_{3\pi/2}^{0.2288\pi}\right)$$

$$C_{L_{2D_{aft}}} = r_{aft}\left(\left(0.7526-0\right)+4\left[-\frac{3}{4}\left(0.7526-0\right)+\frac{1}{12}\left(0.5527-0\right)\right]\right)$$

$$C_{L_{2D_{aft}}} = r_{aft}\left(0.7526-2.2578+0.1842\right) = -1.3210\left(39.5301\text{ in}\right)$$

$$= -52.2193\text{ in} = -4.3516\text{ ft}$$

$$\therefore \frac{C_{L_{2D_{aft}}}}{\text{ft}} = -4.3516$$

For Region II:

$$C_{p_{circ}} = 1-4\sin^2\left(\frac{3\pi}{2}\right) = -3$$

$$C_{L_{2D_{flat}}} = -3L = -3\left(4.0208\text{ ft}\right) = -12.0625\text{ ft}$$

$$\therefore \frac{C_{L_{2D_{flat}}}}{\text{ft}} = -12.0625$$

The two-dimensional lift for each region, and thus the total two-dimensional lift, can then be determined:

$$L_{2D_{fwd}} = qC_{L_{2D_{fwd}}} = -1.875q\text{ lbs/ft}$$

$$L_{2D_{aft}} = qC_{L_{2D_{aft}}} = -4.3516q\text{ lbs/ft}$$

$$L_{2D_{flat}} = qC_{L_{2D_{flat}}} = -12.0625q\text{ lbs/ft}$$

$$L_{2D_{pod}} = q\left(C_{L_{2D_{fwd}}} + C_{L_{2D_{flat}}} + C_{L_{2D_{aft}}}\right)$$

$$= q\left(-1.875-12.0625-4.3516\right) = -18.2891q\text{ lbs/ft}$$

$$\therefore \frac{L_{2D_{pod}}}{\text{ft}} = -18.2891\text{ lbs}$$

Multiplying this result by the pod span yields a three-dimensional lift value:

$$L_{pod} = qbL_{2D_{pod}} = q\left(3.4267\right)\left(-18.2891\right) = -62.6713q\text{ lbs}$$

The three-dimensional potential flow theory pod lift coefficient can then be determined:

$$S_{pod_{theory}} = b_{pod} c_{pod} = (3.4267 \text{ ft})(7.625 \text{ ft}) = 26.1284 \text{ ft}^2$$

$$C_{L_{pod}} = \frac{L_{pod}}{q S_{pod_{theory}}} = \frac{(-62.6713q \text{ lbs})}{(26.1284 \text{ ft}^2) q} = -2.3986$$

APPENDIX A2
CFD ANALYSIS SPECIFICATIONS

CFD analysis for the MAPIR Pod was conducted using SolidWorks Flow Simulation 2009, SP1. The analysis was executed on two personal computers with the specifications listed in table A2.1.

Figure A2.1 illustrates the geometry of the model used in the CFD analysis and the size of the computational domain.

Table A2.1 – CFD PC Specifications for MAPIR Pod Analysis		
	CFD PC 1	CFD PC 2
Manufacturer	Dell	Dell
Model	Precision T7400	Precision T7400
Operating System	Microsoft Windows XP Professional x64 Edition, Version 2003, SP2	Microsoft Windows Vista Business
Processor	Intel Xeon X5472 @ 3.00 GHz	Intel Xeon X5430 @ 2.66 GHz
RAM	32.0 GB	32.0 GB

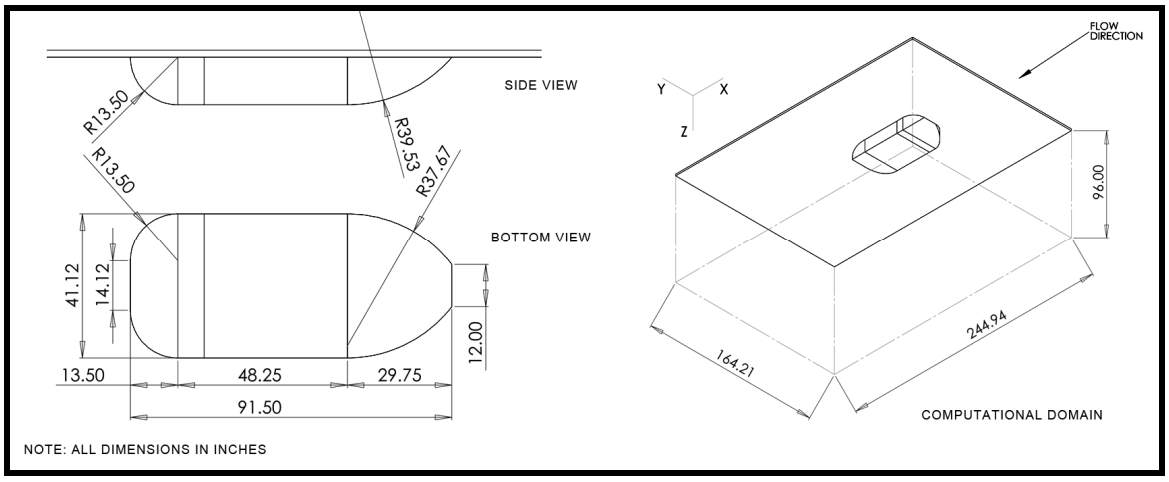

A2.1 – CFD Analysis Geometry

All the MAPIR Pod simulation cases were run at standard sea-level atmospheric conditions. Table A2.2 summarizes the cases tested.

Table A2.2 – Summary of MAPIR Pod CFD Cases					
Velocity (MPH)	Angle of Attack (deg)	Iterations	Velocity (MPH)	Angle of Attack (deg)	Iterations
75	0	2516	175	0	2281
	2	3896		2	5336
	4	4500		4	5869
	6	7533		6	6244
	8	7991		8	9336
	10	7582		10	8367
100	0	2301	200	0	2477
	2	3999		2	6047
	4	4584		4	6917
	6	7510		6	7909
	8	8232		8	9011
	10	8289		10	7725
125	0	2501	225	0	2469
	2	5608		2	5861
	4	6053		4	7730
	6	8613		6	10849
	8	8641		8	9640
	10	8929		10	11346
150	0	2480	250	0	2471
	2	5772		2	7919
	4	6160		4	7815
	6	8146		6	10734
	8	8942		8	11429
	10	9117		10	10666

APPENDIX A3
FLIGHT TESTING

Angle of Sideslip Calibration

The angle of sideslip calibration used for the MAPIR Pod analysis was that detailed by Lawford and Nippress in Reference 9 for calibrating flush air-data systems using dynamic maneuvers. The relevant discussion from this reference is detailed below.

The calibration assumes that the measured sideslip angle β_{meas} is a linear function of the true sideslip angle β_{true}:

$$\beta_{meas} = \beta_0 + K\beta_{true}$$

The time-rate-of-change of sideslip $\dot{\beta}$ as a function of the aircraft flight state is given by:

$$\dot{\beta} = \frac{g_0}{V_{true}} a_y + p\sin\alpha - r\cos\alpha + \frac{g_0}{V_{true}}\cos\theta\sin\phi$$

This term includes both offset errors and random errors; integrating it with respect to time negates the random errors, yielding a nominal true sideslip angle:

$$\beta_{true} = \int [\frac{g_0}{V_{true}}\left(a_y + a_{y_b}\right) + \left(p + p_b\right)\sin\left(\alpha + \alpha_b\right) - \left(r + r_b\right)\cos\left(\alpha + \alpha_b\right) + \frac{g_0}{V_{true}}\cos\left(\theta + \theta_b\right)\sin\left(\phi + \phi_b\right)]dt$$

If the velocity is held constant, expanding the terms and removing higher-order terms gives:

$$\beta_{true} = \int\left[\frac{g_0}{V_{true}}\left(a_y + p\sin\alpha - r\cos\alpha + \cos\theta\sin\phi\right)\right]dt + \int\frac{g_0}{V_{true}}\left(\dot{a}_{y_b} + \phi_b\cos\phi\cos\theta - \theta_b\sin\phi\sin\theta\right)dt + \int\left[\left(p\alpha_b - r_b\right)\cos\alpha + \left(r\alpha_b + p_b\right)\sin\alpha\right]dt$$

The first integral is the nominal true sideslip, and the second two integrals are error terms.

By maintaining a constant airspeed, the changes in both α and θ remain small; thus, they may be replaced by their average values in the second integral:

$$\alpha \approx \bar{\alpha} \qquad \theta \approx \bar{\theta}$$

$$\beta_{true} = \int\dot{\beta}dt + \left[\frac{g_0}{V_{true}}a_{y_b} + p_b\sin\bar{\alpha} - r_b\cos\bar{\alpha}\right]\int dt + \alpha_b\cos\bar{\alpha}\int pdt + \alpha_b\sin\bar{\alpha}\int rdt + \frac{g_0}{V_{true}}\cos\bar{\theta}\int\cos\phi dt - \theta_b\sin\bar{\theta}\int\sin\phi dt$$

At small pitch angles, and thus angles of attack, the products $\theta_b\sin\theta \approx \alpha_b\sin\alpha \approx 0$. Therefore:

$$\beta_{true} = \int \dot{\beta} dt + \left[\frac{g_0}{V_{true}} a_{y_b} + p_b \sin\bar{\alpha} - r_b \cos\bar{\alpha} \right] \int dt$$
$$+ \alpha_b \cos\bar{\alpha} \int p dt + \frac{g_o}{V_{true}} \cos\bar{\theta} \int \cos\phi dt$$

or,

$$\beta_{true} = \int \dot{\beta} dt + C_1 \int dt + C_2 \int p dt + C_3 \int dt$$

where

$$\beta_0 = \int \dot{\beta} dt$$

$$C_1 = \frac{g_0}{V_{true}} a_{y_b} + p_b \sin\bar{\alpha} - r_b \cos\bar{\alpha}$$

$$C_2 = \alpha_b \cos\bar{\alpha}$$

$$C_3 = \frac{g_o}{V_{true}} \cos\bar{\theta}$$

Combining this result with the linear relationship assumed at the outset of the analysis yields:

$$\beta_{meas} = \beta_0 + K\beta_{true}$$

$$\beta_{meas} = \beta_0 + K\beta_{true} - C_1 \int dt - C_2 \int p dt - C_3 \int dt = \beta_0 + K\beta_{true} + (\text{Error Terms})$$

Therefore, the calibration curve for the true sideslip is given by the equation:

$$\beta_{true} = \frac{1}{K}(\beta_{meas} - \beta_0)$$

These equations can be programmed into a numerical solver to process flight test data; this was done for the MAPIR Pod flight testing using MATLAB 2009 and Simulink. *K* must be determined from linear regression of the test data; results from the MAPIR Pod flight testing can be seen in figure A3.1.

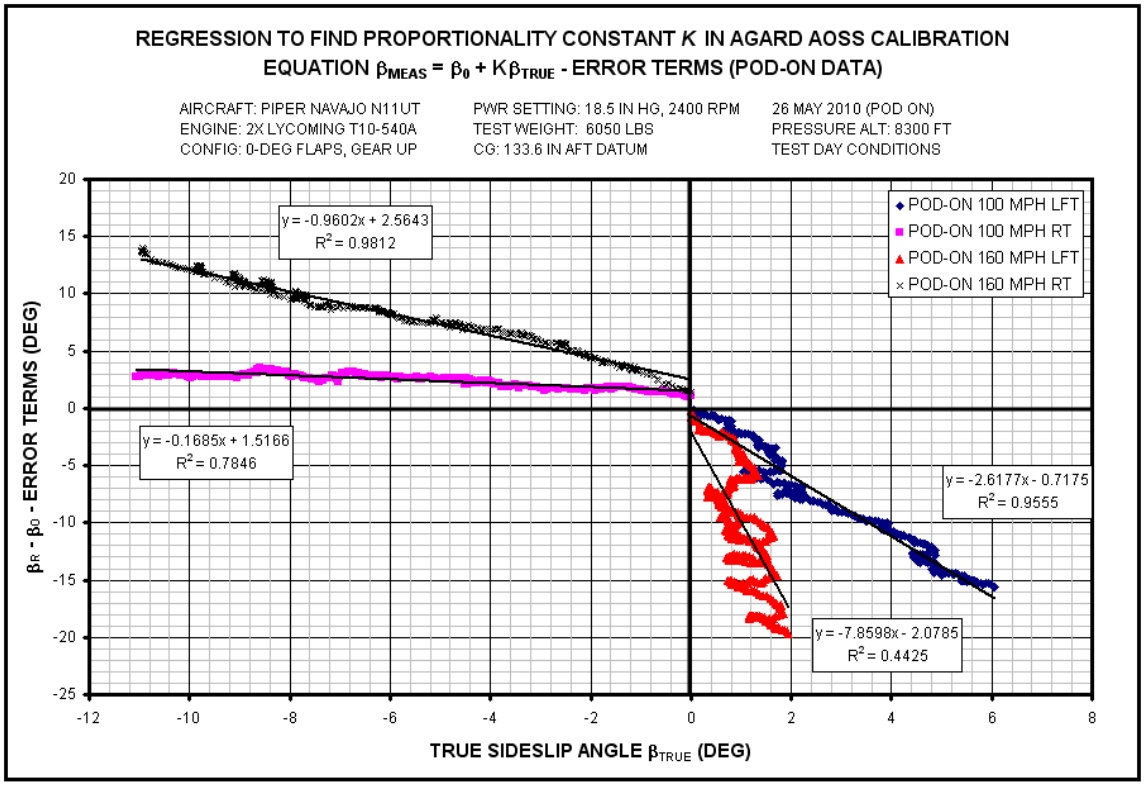

Figure A3.1 – Regression to Find Proportionality Constant *K* in AGARD AOSS Calibration Equation $\beta_{meas} = \beta_0 + K\beta_{true}$ – *Error Terms* (Pod-on Data)

Engine Performance Graphs

Figures A3.2, A3.3, and A3.4 are reproductions of Lycoming performance graphs for the T10-540A engine, which was the engine installed on the test aircraft used for the MAPIR Pod flight testing.

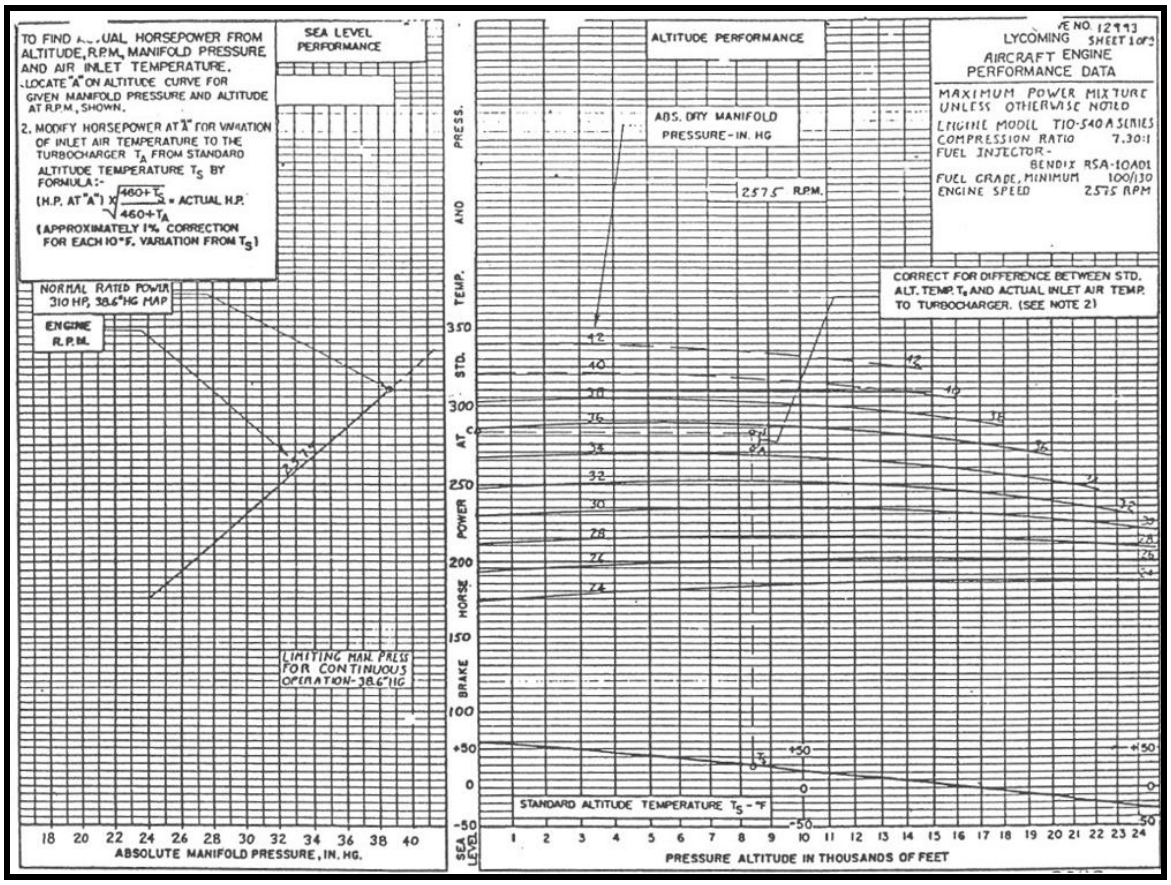

Figure A3.2 – Lycoming Aircraft Engine Performance Data – 2575 RPM

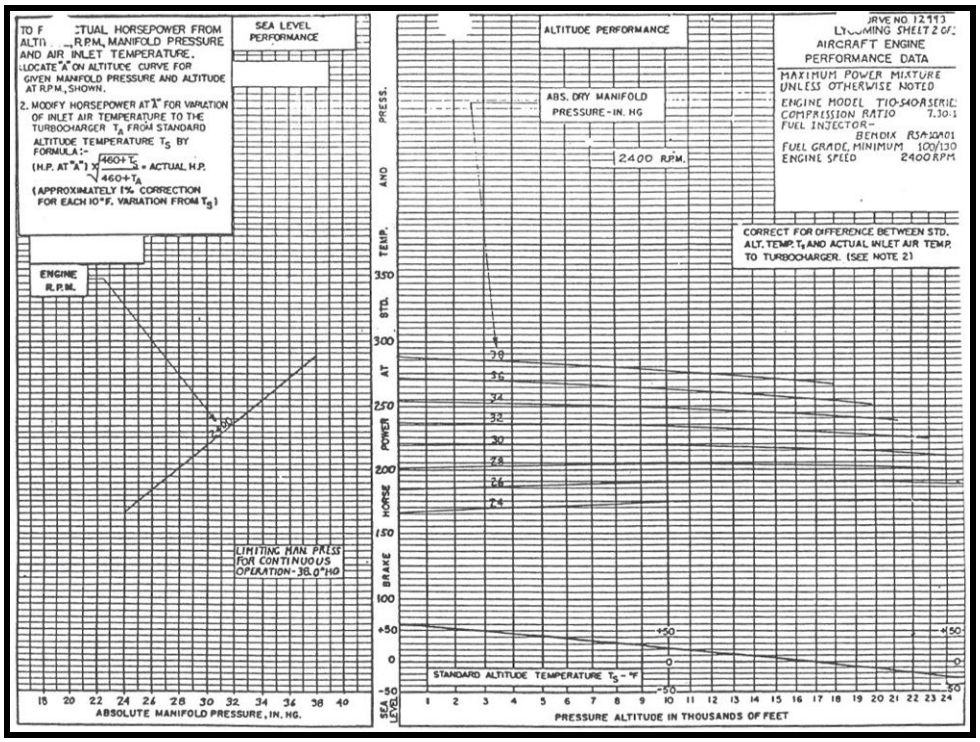

Figure A3.3 – Lycoming Aircraft Engine Performance Data – 2400 RPM

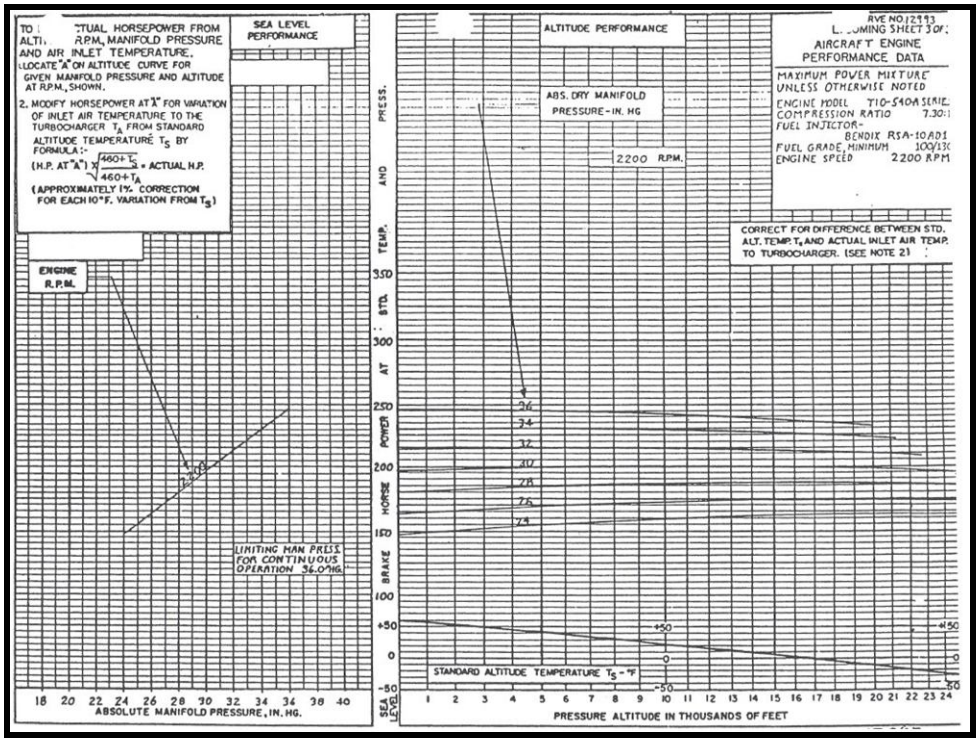

Figure A3.4 – Lycoming Aircraft Engine Performance Data – 2200 RPM

Sample Flight Test Calculations

The following discussion documents the process to calculate the coefficient of lift and coefficient of drag for a single airspeed using data collected during the MAPIR Pod flight testing.

The test weight is found from:

$$\begin{aligned} W_{test} &= W_{empty} + W_{crew} + W_{fuel} \\ &= (4904 \text{ lbs}) + (750 \text{ lbs}) + (6.02 \text{ lbs/gal})(110 \text{ gal}) \\ &= 6316.2 \text{ lbs} \end{aligned}$$

An instrument correction must be applied to the indicated airspeed:

$$\begin{aligned} V_{ic} &= -0.0001V_i^2 + 0.0089V_i - 0.7167 \\ &= -0.0001(143 \text{ kts})^2 + 0.0089(143 \text{ kts}) - 0.7167 \\ &= -1.49 \text{ kts} \end{aligned}$$

$$V_{ic} = V_i + \Delta V_{ic} = (143 \text{ kts}) + (-1.49 \text{ kts}) = 141.51 \text{ kts}$$

This instrument-corrected airspeed is then weight-standardized:

$$V_{iw} = \sqrt{\frac{W_{ref}}{W_{test}}} V_{ic} = \sqrt{\frac{(6500 \text{ lbs})}{(6316.2 \text{ lbs})}} (141.51 \text{ kts}) = 143.56 \text{ kts}$$

A position error must be applied to the weight-standardized airspeed:

$$\begin{aligned} \Delta V_{pc} &= -0.0018V_{iw}^2 + 0.5369V_{iw} - 37.538 \\ &= -0.0018(143.56 \text{ kts})^2 + 0.5369(143.56 \text{ kts}) - 37.538 \\ &= 2.44 \text{ kts} \end{aligned}$$

$$V_c = V_{iw} + \Delta V_{pc} = (143.56 \text{ kts}) + (2.44 \text{ kts}) = 146.00 \text{ kts}$$

An instrument correction must also be applied to the indicated pressure altitude:

$$\begin{aligned} \Delta H_{ic} &= 8 \times 10^{-8} H_p^2 + 0.0007 H_p - 6.8615 \\ &= 8 \times 10^{-8} (8410 \text{ ft})^2 + 0.0007 (8410 \text{ ft}) - 6.8615 \\ &= 4.68 \text{ ft} \end{aligned}$$

$$H_{ic} = H_p + \Delta H_{ic} = (8410 \text{ ft}) + (4.68 \text{ ft}) = 8414.7 \text{ ft}$$

A position error must be applied to this new altitude reading:

$$\begin{aligned} \Delta H_{pc} &= -0.0066V_{iw}^2 + 2.854V_{iw} - 231.86 \\ &= -0.0066(143.56 \text{ kts})^2 + 2.854(143.56 \text{ kts}) - 231.86 \\ &= 41.83 \text{ ft} \end{aligned}$$

$$H_c = H_{ic} + \Delta H_{pc} = (8414.7 \text{ ft}) + (41.83 \text{ ft}) = 8456.5 \text{ ft}$$

The temperature ratio at altitude is given by:

$$\theta = \frac{(OAT + 459.7)}{518.7\ \text{K}} = \frac{(34.27\ ^\circ\text{C}) + (459.7\ ^\circ\text{C/K})}{518.7\ \text{K}} = 0.8887$$

The pressure ratio at altitude is found from:

$$\delta = \left(1 - 6.875 \times 10^{-6} H_c\right)^{5.2561}$$

$$= \left(1 - 6.875 \times 10^{-6} (8456.5\ \text{ft})\right)^{5.2561} = 0.7299$$

The density ratio can then be determined:

$$\sigma = \frac{\delta}{\theta} = \frac{0.7299}{0.8887} = 0.8213$$

The density at the test point is then easily found from:

$$\rho_{test} = \sigma \rho_0 = 0.8213(0.002377\ \text{slug/ft}^3) = 0.001952\ \text{slug/ft}^3$$

The true airspeed at the test point is then:

$$V_{true} = \frac{V_c}{\sqrt{\sigma}} = \frac{(146.00\ \text{kts})}{\sqrt{(0.8213)}} = 161.10\ \text{kts}$$

Using an RPM of 2400, a manifold pressure of 30.2 in Hg, and an inlet temperature of 3.67 ˚C, figure A3.3 gives a power output of 219.15 HP for the left engine. Similarly, using an RPM of 2400, a manifold pressure of 29.4 in Hg, and an inlet temperature of 13.6 ˚C, figure A3.2 gives a power output of 209.27 HP for the right engine.

These power settings can then be used in conjunction with the true airspeed, RPM, OAT, calibrated pressure altitude, and test point density to find the engines' thrust. Reference 1 gives a left engine thrust of 363.44 lbs and a right engine thrust of 349.27 lbs with these values.

The total thrust is the sum of the individual engines' thrusts:

$$T_{total} = T_{left} + T_{right} = (363.44\ \text{lbs}) + (349.27\ \text{lbs}) = 712.71\ \text{lbs}$$

The lift is then found from the test point weight and the aircraft's pitch and roll attitudes:

$$L = W_{test} \cos\theta \cos\phi - T_{total} \sin\theta$$

$$= (6316.2\ \text{lbs}) \cos(1.99\ \text{deg}) \cos(0.889\ \text{deg}) - (712.71\ \text{lbs}) \sin(1.99\ \text{deg})$$

$$= 6287\ \text{lbs}$$

The drag is found from the total thrust and the pitch attitude. The flight testing was conducted at zero sideslip angles and in steady flight, where the pitch attitude equaled the angle of attack. Thus:

$$D = T_{total} \cos\theta = (712.71\ \text{lbs}) \cos(1.99\ \text{deg}) = 712.28\ \text{lbs}$$

The coefficient of lift can then be given by:

$$C_L = \frac{L}{\frac{1}{2}\rho_{test} V_{true}{}^2 S_{ref}}$$

$$= \frac{(6287 \text{ lbs})}{\frac{1}{2}\left(0.001952 \text{ slug/ft}^3\right)\left[(161.10 \text{ kts})\left(\frac{6076}{3600}\ \frac{\text{ft/s}}{\text{kts}}\right)\right]^2 \left(229 \text{ ft}^2\right)}$$

$$= 0.3804$$

The coefficient of drag is similarly found:

$$C_D = \frac{D}{\frac{1}{2}\rho_{test} V_{true}{}^2 S_{ref}}$$

$$= \frac{(712.28 \text{ lbs})}{\frac{1}{2}\left(0.001952 \text{ slug/ft}^3\right)\left[(161.10 \text{ kts})\left(\frac{6076}{3600}\ \frac{\text{ft/s}}{\text{kts}}\right)\right]^2 \left(229 \text{ ft}^2\right)}$$

$$= 0.0431$$

VITA

Will Moonan grew up in Bedford, MA. He attended grade school in his home town, and graduated from Concord Academy in Concord, MA in 2004. Will then attended Rice University in Houston, TX, graduating with a Bachelors of Science in Mechanical Engineering in 2008. From there, he worked as a Graduate Research Assistant while studying at the University of Tennessee Space Institute in Tullahoma, TN. Will has worked on airborne science missions with both NASA and NOAA while working at the University of Tennessee Space Institute.

Will is currently pursuing his Masters of Engineering Science, concentrating in Flight Test Engineering, from the University of Tennessee Space Institute. In January, 2010, he will begin work with QinetiQ North America as a Flight Test Engineer supporting the United States Army Flight Test Directorate at Redstone Arsenal in Huntsville, AL.